University of Seville

Department of Condensed Matter Physics

Ph Dissertation prepared by Yoshihiro Tamura to fulfill the requirements for the award of the Doctorate Degree from the University of Seville by appointment of His Majesty the King Philip VI of Spain

Advisors

Dr. Eugenio Zapata Solvas   Dr. Bibi Malmal Moshtaghion Entezari

University College London, United Kingdom   *University of Zaragoza, Spain*
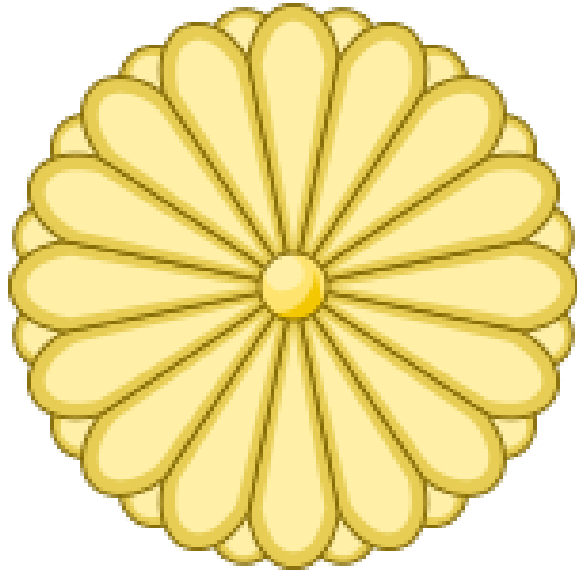
Coordinator

Dr. Diego Gómez García

University of Seville, Spain

Seville, November 2018

FABRICACIÓN Y PROPIEDADES MECÁNICAS DE NUEVOS MATERIALES A BASE DE ALÚMINA REFORZADOS CON FIBRAS DE ALÚMINA

FABRICATION AND MECHANICAL PROPERTIES OF ALUMINA WHISKER-REINFORCED ALUMINA-BASED NEW MATERIALS

INDEX

Prologue: *Main research goal and a general view of the dissertation. Some specific experimental techniques which are not currently available.*

Chapter 1. *New aspects on the sintering of alumina polycystals by spark plasma sintering and the diffusion of alumina along the grain boundaries.*

Chapter 2: *Sintering of alumina-whisker-reinforced alumina composites. General conditions. Microstructural characterization. Room-temperature fracture properties.*

Chapter 3: *On the high-temperature plasticity of alumina-whisker-reinforced alumina composites. Microstructural characterization. Modelling of the deformation mechanisms.*

Chapter 4: *Conclusions and prospective in this research line.*

RESUMEN DE LA TESIS

Este trabajo de investigación se enmarca dentro de la ambiciosa línea de investigación de nuevos materiales cerámicos compuestos con aplicaciones tecnológicas. El objetivo ha consistido en la fabricación de un material cerámico compuesto de forma reproducible mediante la técnica de sinterización por chispa de plasma, y su posterior caracterización mecánica y microestructural ante esfuerzos mecánicos a temperatura ambiente y a altas temperaturas. El material objetivo de esta memoria ha sido un material compuesto basado en alúmina policristalina reforzada con fibras de alúmina.

Dos ideas leit-motivs han precedido a esta elección: la alúmina es, junto con la circonia itriada y la magnesia, el material cerámico por excelencia en el mundo tecnológico actual. Como es bien sabido, el mercado es eminentemente conservador y sólo tras muchas pruebas acepta reemplazar un material que ha resultado exitoso con creces. Parece una buena idea intentar mejorar la alúmina…..con fibras de alúmina igualmente. Es evidente que muchas propiedades positivas de la alúmina van a permanecer inalteradas y a priori es plausible pensar que las propiedades mecánicas pueden resultar mejoradas. En particular, la alúmina es de suyo un material con una resistencia a la oxidación y a la corrosión que obviamente van a quedar incólumes.

Por otra parte, el estudio de la resistencia a la fractura y de la plasticidad a altas temperaturas es a primera vista un objetivo atractivo: no se ve afectado por la formación de terceras fases, fases vítreas o reacción en las fronteras de grano. Es desde el punto de vista teórico, un problema de redistribución de tensiones en el interior del material, que altera el posible deslizamiento de las fronteras de grano durante la solicitación mecánica.

5

En esta memoria se describen, en primer lugar, las condiciones de optimización del sinterizado mediante chispa de plasma de policristales de alúmina. Con posterioridad se reportan las condiciones para la fabricación de composites reforzados de alúmina en forma reproducible.

En los siguientes capítulos se estudian las propiedades de fractura a temperatura ambiente y plasticidad a altas temperaturas, procediendo a la modelización de ambos fenómenos.

Los resultados prueban que estos composites son muy ventajosos tanto a altas como a bajas temperaturas y son una alternativa viable y poco costosa para reemplazar sistemas compuestos más exóticos, más costosos (como los basados en nanotubos de carbono o grafeno) pero con escasa reproducibilidad.

ACKNOWLEDGEMENTS

From a personal point of view, I want to express my gratitude to all the professors who have welcomed me and my wife at the University of Seville. Special thanks are dedicated to my advisor and co-supervisors for their help and encouragement during the long process of PhD preparation and writing. I want to add my sincere acknowledgement to Prof. Arturo Domínguez Rodríguez, who motivated a great deal to resume with this exciting research topic.

Special thanks are transmitted to Prof. Ángel Luis Ortiz Seco for his help with the composite preparation and to Prof. Guitian's team in Universidad de Santiago de Compostela aned Neoker Company, Spain for the supply of alumina whiskers.

Prologue

Main research goal and a general view of the dissertation. Some specific

experimental techniques which are not currently available.

Summary

This brief introduction presents the objective of this dissertation, the structure of the manuscript and finally it revises different experimental techniques (either mechanical testing tools or microscopic analysis of microstructure) required for the development of this research work.

P1: Main hypothesis, research target and strategy.

The specific singularity of the human species is the ability to fabricate tools and modify the environment. For the modern Antropology, the culture in the human being is intrinsically connected to the ability of fabricating items to satisfy physiological or spiritual needs. The pure "Natürmensch" does not exist. In other words, the intelligence of humans is closely connected to materials. Materials are ubiquitous in modern societies: they are critical for transportation, industrial infrastructure, components in technological devices for health care, prosthesis for damaged bones, equipments to use and save energy and so on. The life standard in modern societies depends on the ability to innovate new materials for more and more demanding needs. Up to now, our industry has been based upon the access to strategic metals and energy sources. The history of the twentieth Century cannot be explained if we ignore the location of fuel, coal, steel jut to say a few materials. The Second World War or the history of Middle East battles are also the wars for the supply of essential materials for armies and industry. Over the first decades of the new century, this statement is still a reality: the search of materials with attractive properties, easy fabrication and well distributed all over the earth is a leit-motiv for economic and political reasons.

In this context, ceramics in general and alumina in particular play a key role. Ceramics are cheap, very hard, abundant on earth, excellent high-temperature materials and resistant to corrosion. Unfortunately they are brittle. Overcoming this drawback is a goal of all modern ceramist. Alumina and zirconia are by far the most studied and used advanced ceramic materials. Alumina is the first demanded ceramic material for the Japanese industry and there is clearly a growing tendency for the next decades. The mechanical and fracture properties of alumina ceramics have been the subject for a very intense research program for the last forty years. This also includes the use of different

10

sintering and fabrication of complex pieces. The number of research papers reporting basic properties of alumina ceramics and/or new sintering techniques as well as alumina-based composites is very high: this topic is one of the main topics of the Ceramic Science. Among the new sintering techniques, a new one has been consolidated as a fruitful one: the spark plasma sintering (SPS) or electric field-induced sintering techniques in general. There are numerous papers reporting the sintering and consolidation of fine-grained pieces of different alumina powders.

At this regard, searching for innovation in alumina is a priori a very difficult goal. This dissertation is aimed at making a new contribution to the world of the science and technology of alumina.

Despite the numerous examples of alumina-based ceramic composites, there is one obvious one which has been forgotten: we mean alumina-fiber-reinforced alumina. This is a simple option which very straightforward advantages: there is no problem of chemical compatibility between the components of the composite. For sure it is going to be a corrosion-resistant and oxidation-resistant composite. A basic question arises: is it a good choice in terms of mechanical properties? We have made the hypothesis of accepting a positive reply to this question. This thesis tries to elucidate whether this reply is right or wrong. To this end, we have determined the optimal conditions for SPS fabrication of these composites. Later on, their microstructure has been characterized and they have been tested at room-temperature as well as high-temperature conditions to determine their fracture and plastic properties respectively.

This dissertation is organized in a rather non-conventional way. It is shortened to emphasize what is really new on the research in these alumina composites. The structure of the manuscript follows closely the publications in JCR journal on different aspects of

the fabrication, mechanical testing and modeling of alumina-fiber-reinforced alumina ceramics.

Chapter 1 is devoted to the description of the SPS sintering procedure. This is a well-established issue. The chapter concentrates on two problems which have been ignored so far: one of them is the analysis of the real temperature on the ceramic powder when a value of the temperature at the pyrometer has been settled. At the same time, the role of the heating rate on the final density of the ceramic pieces has been précised. The other one concerns the matter transport during sintering, i.e. the value of the diffusion coefficient of the slowest species while sintering. Such diffusion coefficient has been determined and it is clearly in disagreement with those previously reported in literature through other techniques. In this chapter we will put forward the importance of the recently discovered disconnections as a driving force for grain growth in alumina, particularly when electric fields are present. We will prove that, when such fields are properly considered in the kinetics law, the corrected diffusion coefficient is consistent with those reported in the past.

Chapter 2 is focused on the fabrication and analysis of the hardness and fracture toughness of our alumina-based alumina composites. Similarly, chapter 3 is dedicated to the study of the high-temperature plasticity, creep resistance and modeling of the mechanism leading grain boundary sliding in our composites.

Finally, chapter 4 concludes our results and points out several pending questions and future work to be done.

The following sections in this prologue are a brief summary or some basic experimental techniques which have been used preferentially along this research work.

NOTE TO THE READER

The fabrication procedure of alumina whiskers is not described in this dissertation book because it is protected under patent owned by Neoker, a branch of the Advanced Composite Materials Research Center, Tsinghua Innovation Center in Dongguan, China.

13

P2- Densification by Spark Plasma Sintering (SPS)

All different kinds of powders were consolidated under vacuum in a SPS device (Dr. Sinter 515S, Kanagawa, Japan). The unit consists of a sample chamber with hydraulic rams, graphite spacers, graphite die and punch (Fig P1), a power unit, water cooling circuit, control module, and computer data acquisition unit (Fig. P2). The data acquired during the SPS process included time, temperature, current, voltage, and displacement. In all experiments, the ceramic powder was loaded into a 15-mm diameter graphite die lined with graphite foil and surrounded by a 1 cm thick graphite blanket to minimize heat loss, and then spark-plasma sintered in a dynamic vacuum (i.e., ~6 Pa) at peak temperatures in the set temperature (as measured by an optical pyrometer focused on the die), with dwell times in the interval 1–10 min, heating ramps of 100-300°C/min on request, and uniaxial pressure of 75 MPa (applied since the first minute of heating). The conditions of all experiments by SPS are provided in corresponding experimental sections in the following chapters.

The applied electrical power is applied by the SPS in rapid pulses of 3.3 ms. The applied voltage is in the range 0–10 V, while the current can be as high as 2000 A in our system. The pulses are provided in groups of up to 99 consecutive pulses, followed by 1–9 missing pulses. The sequence represents the pulse pattern. In this research work a pulse pattern of 12:2 (12 pulses on and 2 off) was always used.
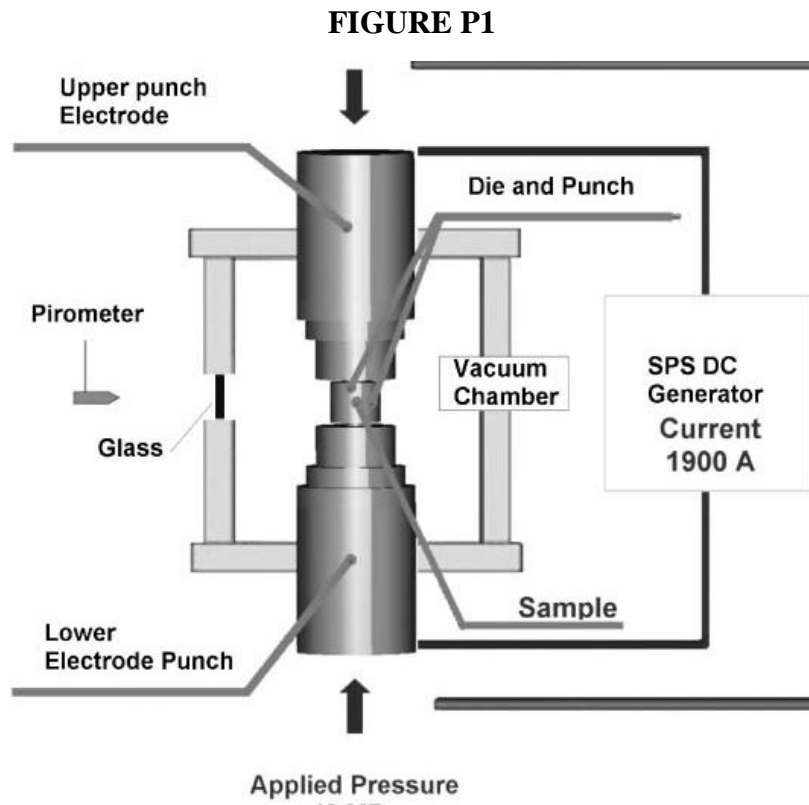
14

FIGURE P1

Fig. P1- Schematic of a SPS device.

FIGURE P2

Fig. P2. Spark plasma sintering machine available at the University of Seville labs.

P3- Characterization after SPS consolidation: main techniques

P3.1- Density measurement

The density of sintered samples was measured by the distilled water displacement technique (Archimedes method). According to the Archimedean Principle, a solid body immersed in a liquid apparently loses as much of its own weight as the weight of the liquid that it has displaced. This makes it possible to determine the unknown value. For this propose, the samples were first weighted in air, and then immersed. And from the two weightings (made in grams), density ρ was calculated by Equation P1:

$$\rho = \frac{W_d}{W_d - W_{sub}} \times \rho_0 \qquad (1)$$

Where ρ [g/cm^3] is the density of the sintered samples, ρ_0 is the density of distilled water at room temperature, W_d [g] is the weight of samples in air (dry weight) and W_{sub} [g] is the weight when immersed in distilled water. Hence (W_d-W_{sub}) equals the buoyancy in grams.

P3.2- X-ray diffraction

X-ray bulk diffraction (XRD) of the samples was carried out by X-ray diffractometry (XRD; D8 Discover, Bruker, Germany) to analyze the structural changes of the sintered samples. Diffraction patterns were recorded using the Cu Kα radiation over a 2θ range of 10–90∘ and a position-sensitive detector using a step size of 0.05˚ on the polished cross-section surface of samples. In order to determine the crystallographic data and accurate compositions of sintered samples in different conditions, Rietveld refinement was performed. In this study, we used the version 3.5d of the Rietveld analysis software FULLPROF[89], assuming the pseudo-Voigt function to describe the peak shapes. The

refinement protocol included the background, the scale factors, and the global-instrumental, lattice, profile and texture parameters.

P3.3- Microstructural observations.

P3.3.1-Scanning Electronic Microscope (SEM) and High-Resolution Scanning Electronic Microscope (HRSEM)

Microstructural analysis was performed on both fractured and polished surfaces of all the sintered and deformed samples by Scanning Electron Microscopy (Philips XL30, The Netherlands) and High-Resolution Scanning Electron Microscopy (HRSEM; S5200, Hitachi, Japan) for sub-micrometric and ultra-fine microstructures, respectively. In the required cases X-ray energy dispersive spectrometry (XEDS) coupled to SEM was used for chemical determination of different observed grains. For observing polished surfaces (1-µm finish using routine ceramographic methods), no electro-chemically etching is necessary. The average grain size D was determined from the SEM images. To this purpose, the grain diameter was defined as that of the equivalent circle as follows:

$$D = 2\sqrt{\frac{Area}{\pi}} \qquad (2)$$

P3.3.2- Transmission Electronic Microscope (TEM)

TEM observation was performed by means of Hitachi H800 or Philips CM-200 microscopes operated at 200 kV in order to study the microstructural evolution at the scale of individual grains, especially after deformation tests. In TEM, slices from sintered samples before and after creep testing were prepared using conventional TEM-specimen-preparation methods. All foils were mechanically ground to a thickness of about 100 µm and polished with diamond paste of grain size 3 µm. They were then

17

dimpled to ~30 µm (Dimpler grinder Gatan Model-656) and ion-beam-thinned to electron transparency (PIPS Gatan Model-691).

P4- Mechanical properties at room temperature

P4.1- Vickers Hardness

Hardness was measured by the Vickers indentation test. In the materials community Vickers hardness in general is used for measuring hardness; however it can be used for fracture toughness measurement also. The widely-accepted definition of hardness testing considers the actual area of contact of the four facets of an indenter pyramid leading to a definition of Vickers hardness:

$$H = 2P/a^2 \qquad\qquad (3)$$

where 2a is the length of the diagonal of the hardness indent and P is the applied load. Figure P3 is a scheme of the crack used for Vickers hardness determination.
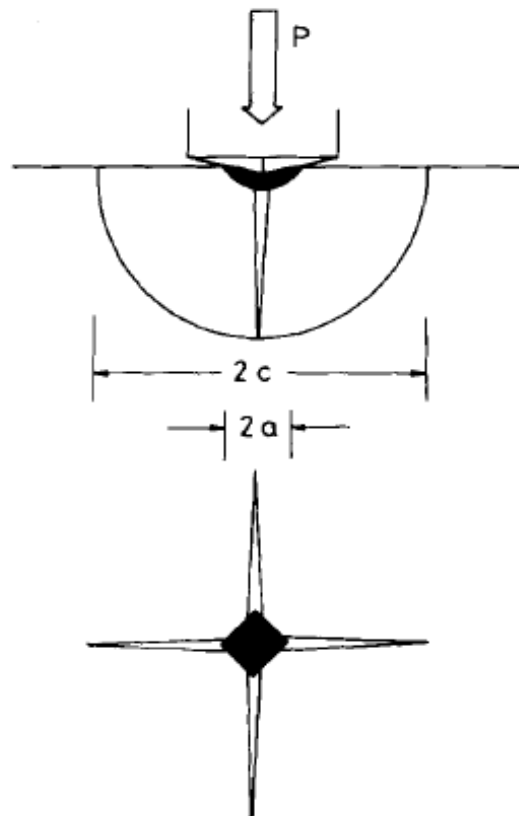
18

FIGURE P3

Fig. P3. Schematic of Vickers-produced indentation-fracture system, peak load *P,* showing characteristic dimensions C and a of radial-median crack and hardness impression, respectively [1].

In this study, polished cross-section of sintered samples were cut along the diameter of the disc-shaped discs and were indented at several locations (minimum 10 indentations per specimen) under a load (P) of 9.81 N using a hardness tester (Struers A/S, DK-2750 Bullerup, Denmark) equipped with a Vickers diamond pyramid. Diagonal lengths of Vickers imprint (2a) were measured by optical microscopy.

P4.2- Fracture toughness by means of Vickers hardness

Cracks extending from the corners of the Vickers indentations were used for fracture toughness (K_{IC}) measurements. The original idea was first proposed in the late 1970´s by Lawn et al [2]. The method has subsequently received much recent attention for making measurements of fracture toughness in different materials. However, accurate measurement of the fracture toughness in brittle materials is still a challenging task. Indeed, creating sharp pre-cracks for measuring toughness in hard ceramics is often difficult without catastrophically failure of the specimen, while fracture toughness data using notched specimens can give erroneously high values. Such tests based upon the Vickers hardness can be relatively quick and easy to perform and require little specialized equipment, and it can provide insight into localized microstructural features. Accordingly, such techniques are finding considerable usage in studying the fracture behavior of hard and brittle materials [2, 3].

Numerous empirical fracture toughness relations are available in literature depending on the nature of the crack systems [4]. It should be mentioned that the way of calculating the fracture toughness is determined by the crack pattern, i.e., either according to a radial/median (half-penny cracks) [2] or Palmkvist crack [5, 6] mode. The radial-median (half-penny) cracks are usually observed on the brittle materials with very limited plasticity and low fracture toughness like ceramics and glasses as well as the high-indentation load when the crack easily propagates along the surface and into the bulk of the specimen. This half-penny crack is characterized by a relatively high ratio of the crack length C to the half-diagonal of the indent C/a≥3 (Fig. 3.7). A number of models for the radial-median crack geometry are suggested and they can be written in the general form:

$$K_{IC}^{\text{Half-penny}} = \beta.(E/H)^n.P.C^{-3/2} \qquad (4)$$

where β and n are dimensionless experimental factors and power constants equal to 0.016 and 0.5, respectively according to Lawn et.al. [1, 2] and E is the Young modulus. The dimensionless factor $(E/H)^n$ in Eq. (4) accounts for the effects of the residual stresses beneath the hardness indentation.

Another crack system, so-called Palmqvist cracks, is considered for low values of *c/a*. Such cracks begin only at the end of the diagonals of the indentation, as illustrated in Fig. P4. In this mode, four independent elongated semielliptical cracks are created with relatively low ratio of the length (L) to the half-diagonal (a) of the indent 0.25≤L/a≤2.5. According to this model fracture toughness can be estimated from the following law:

$$K_{IC}^{\text{Palmkvist}} = 0.0122(E/H)^{2/5} P/aL^{1/2} \qquad (5)$$
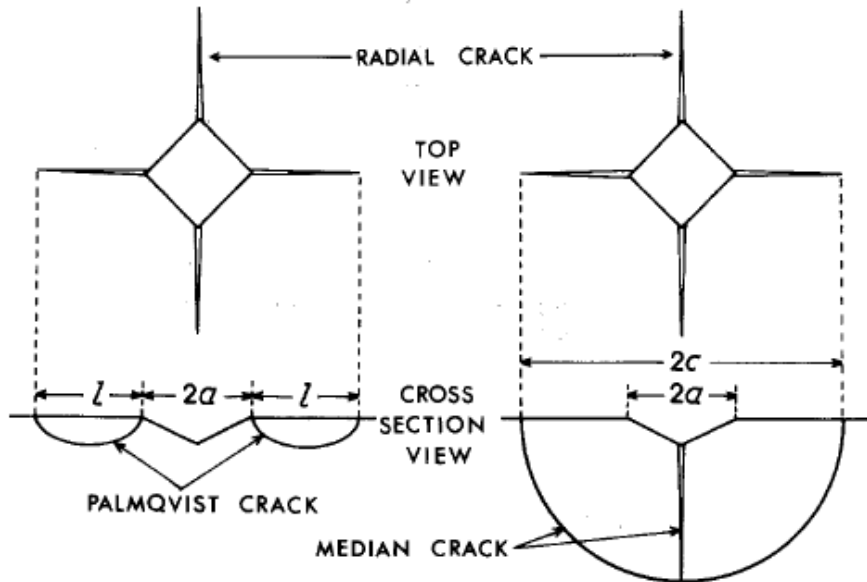
FIGURE P4

Fig. P4. Comparison of geometries of Palmqvist and median cracks around Vickers indentation [5].

Each type of crack configurations results in different values for K_{IC}. In order to identify the most suitable type of crack in a particular case, an additional post-indentation polishing is required. The gap in-between the edge of the polished indentation and the actual crack reveals a Palmqvist crack mode [48, 66]. In the current study, the indented surfaces were additionally polished for few minutes with 3 μm diamond paste and no gap appeared after the subsequent polishing on the indented surfaces. This is consistent with a half-penny crack-type beneath the indentations. The fracture toughness can therefore be calculated according to Eq. (4).

P5-High-temperature mechanical properties

Evaluation of mechanical properties or plastic deformation of ceramics at high temperatures can be performed by means of two different types of deformation tests. One of them is a compression test at constant load which is well-known as a creep test and the other one is a compression test at constant strain rate (cross-head speed) that results in the conventional stress-strain curve. Both cases can be used for determining the mechanical behaviour of ceramics at high temperatures. Data are rationalized in terms of the high-temperature creep equation (Eq. 6):

$$\dot{\varepsilon} = A \frac{Gb}{kT} \left(\frac{\sigma}{G} \right)^n D_0 \exp\left(-Q\beta \right) \tag{6}$$

Where n and Q are the stress exponent and the activation energy respectively, D_0 is the pre-exponential factor of a diffusion coefficient, G is the shear modulus, σ and T are the

22

applied stress and the temperature respectively, k is the Boltzmann's constant, b is a typical length of the microstructure (for instance, the Burgers vectors of dislocations in the material of the lattice parameter) and $\beta=1/kT$. Finally, A is a non-dimensional empirical constant which depends on the microstructure.

In this equation the stress exponent (n) and the activation energy (Q) are important parameters to elucidate the creep mechanism of materials at high temperature. The stress exponent (n) can be easily calculated by jumps in stress at constant temperature in the case of compression test at constant load, while for compression test at constant strain rate it is obtained by change of the strain rate at constant temperature. Activation energy can be calculated by means of temperature changes while the stress or strain rate is kept constant in compression test at constant load or at constant strain rate, respectively.

In this study, compression tests at constant load were used for evaluating of deformation mechanism of alumina-reinforced ceramics. All the experiments were carried out in one prototype machine which is shown in Fig. P5 and Fig. P6.. The required samples for this test are small parallelepipeds of dimensions 2.5 mm × 2.5 mm × 5.0 mm that are positioned between two silicon carbide (SiC) cylinders surrounded by heating elements of tungsten in the center of a chamber (Fig. P6). An upper SiC cylinder or piston is fixed while the lower one is mobile. The required load can be applied by the equivalent weight with a factor 0.1 on a plate attached via a lever system to the lower piston on the sample.

The tests were performed at different range of temperatures under in argon atmosphere. To minimize contamination of furnace walls, several cycles of vacuum followed by introduction of argon at room temperature were done. These cycles were repeated again

23

at 500 ° C to remove the products of the possible degassing of the elements inside the chamber. To avoid possible buckling of the samples with SiC pistons, samples were sandwiched between SiC pads. In these typical tests, changes in the length of the sample were recorded versus the time. Since the original length (l_0) is known, the real strain can be calculated accordingly:

$$\varepsilon(t) = \ln\left(\frac{l_0}{l(t)}\right) = \ln\left(\frac{l_0}{l_0 - \Delta l(t)}\right) \tag{7}$$

where l(t) is the length at a time t and Δl(t) is the change in the length with time . Then the strain rate will be:

$$\dot{\varepsilon} = \frac{d\varepsilon}{dt} \approx \frac{\Delta\varepsilon}{\Delta t} \tag{8}$$

Therefore, the typical creep curve of strain rate versus strain can be drawn. Also real stress can be calculated as a following:

$$\sigma(t) = \frac{F}{S(t)} \tag{9}$$

where F is the applied load and S(t) the surface section. Considering that the volume of sample is constant:

$$S_0.l_0 = S(t).l(t) \tag{10}$$

where S_0 is the original transversal section. According to Eq. 9 and 10, the real stress can be obtained as:

$$\sigma(t) = \frac{F}{S_0 e^{\varepsilon(t)}} = \sigma_{eng} e^{-\varepsilon(t)} \tag{11}$$

FIGURE P5

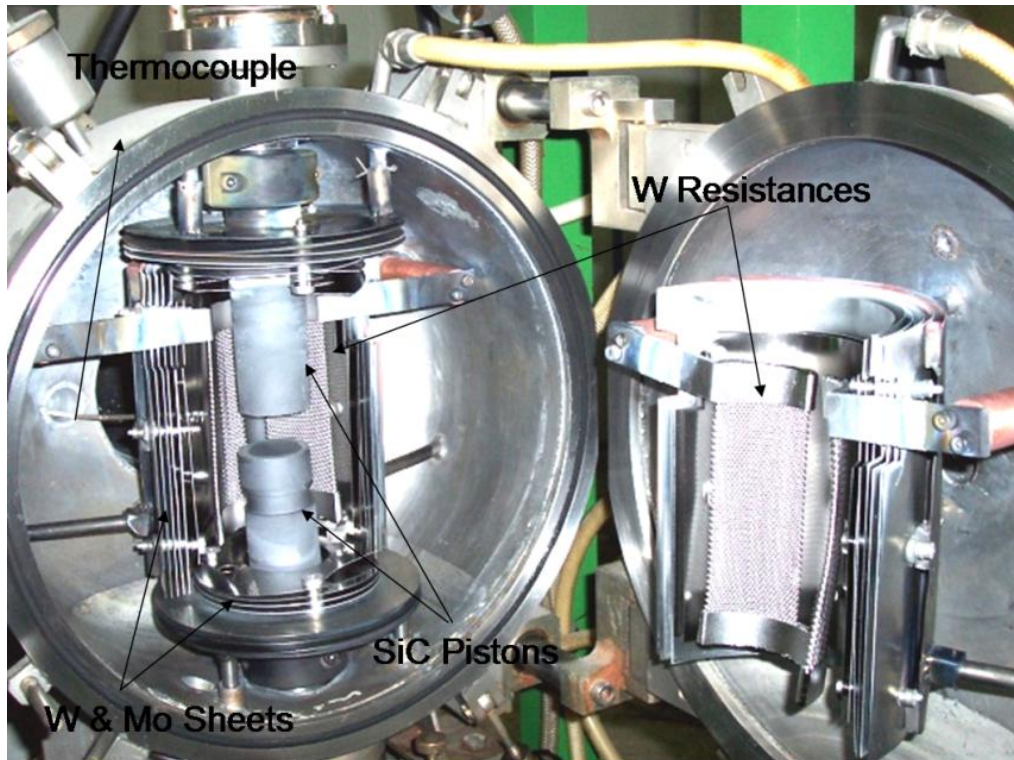Fig. P5. The prototype creep machine used in this study.

FIGURE P6

Fig. P6. Experimental set-up inside the heating chamber of the creep machine.

REFERENCES

[1]-G. R. Anstis., et al., "A critical evaluation of indentation techniques for measuring fracture toughness: I, Direct crack measurments," *J Am Ceram Soc*, 64 533-538 (1981).

[2-]B. Lawn. and R. Wilshaw., "Review Indentation fracture: principles and applications," *J Mater Sci*, 10 1049-1081 (1975).

[3]-J. J. Kruzica., et al., "Indentation techniques for evaluating the fracture toughness of biomaterials and hard tissues," *J Mech Behavior Biomed Mater*, 2 384-395 (2009).

[4]-C. B. Ponton. and R. D. Rawlings., "Vickers indentation fracture toughness test part 1 review of literature and formulation of standardized toughness equations," *Mater Sci Tech*, 5 865-872 (1989).

[5]-K. Niihara., R. Morena., and D. P. A. Hasselman., "Evaluation of K_{IC} of brittle solid by the indentation method with low crack-to indent ratios," *J Mater Sci Lett*, 1 13-16 (1982).

[6]-K. Niihara., "A fracture mechanics analysis of indentation-induced Palmkvist crack in ceramics," *J mater Sci Lett*, 2 221-223 (1983).

Chapter 1

New aspects on the sintering of alumina polycystals by spark plasma sintering and the diffusion of alumina along the grain boundaries.

Summary

The sintering of fine-grained α-alumina by spark plasma sintering (SPS) was performed to study grain growth under SPS conditions. Grain growth is found to be extensive at relative densities above 95%. A grain growth versus dwell time analysis during SPS allows for the determination of the grain-boundary diffusion coefficient. This study shows that the remarkable enhancement of grain-boundary diffusion derived from a previous analysis could be a consequence of the presence of the recently discovered "disconnections" at the grain boundaries of α-alumina. Their presence, together with their electric charge and the external electric field at the boundaries, are the key ingredients for a violation of the typical grain growth kinetic law. When they are introduced appropriately, an updated value of the grain-boundary diffusion coefficient is achieved. A comparison with other values reported previously in the literature through other techniques and a critical analysis are also carried out.

1.1. Introduction

Alumina-based materials have widely attracted the interest of the international science community due to their physical-chemical properties, such as mechanical, electrical and chemical stability and abrasion resistance. Alumina ceramics represent the highest investment in Japanese industry compared to the other ceramic systems [1]. Although alumina is a promising candidate for high temperature structural applications, its brittleness is a limiting factor for a broader range of applications. One classical approach to improve the brittleness and other properties of alumina is the achievement of a fine microstructure [2,3]. In fact, the combined use of a starting powder of fine particles and a controlled sintering process, which could minimize grain growth, may lead to the manufacturing of a dense sintered body with a fine-grained microstructure. One of the most studied processes to control grain size is the use of additives that limit grain growth [4]. However, even a small concentration of additives in a highly stoichiometric compound can generally modify the material properties, such as oxidation resistance, thermal transport or high temperature creep behaviour.

The sintering of dense materials by spark plasma sintering (SPS) has been extensively studied since the early 1990s [5]. The raw material powder is placed in a graphite die and pressed with two graphite punches to a certain pressure in a chamber under vacuum. An electric current is then applied through the mould producing Joule heating. Joule heating enables high heating and cooling rates, which minimize grain growth during sintering, as well as lowering the sintering temperature and dwell time compared to other techniques, such as pressureless sintering or hot pressing [6,7]. Although an explanation for the fundamental mechanism is still under debate, SPS has been intensively investigated by several authors to determine the effect of SPS conditions, such as sintering temperature, sintering dwell time, heating rate and

30

mechanical pressure on the relative density and grain size of alumina [8–14]. The smallest grain size reported in a dense alumina specimen is 0.2 μm, with a relative density of 98%, a sintering temperature of 1550 °C, a dwell time of 2 min and a heating rate of 200 °C/min. The applied mechanical pressure was 100 MPa and a starting alumina powder size of 0.2 μm was used [8]. In the case of relative densities higher than 99.7%, the smallest grain size achieved is 0.3 μm, resulting from a sintering temperature of 1200 °C, a sintering dwell time of 3 min, a heating rate of 150 °C/min and a mechanical pressure of 100 MPa [9]. Aman *et al.* [11] carried out an experimental screening design method with the aim of obtaining an insight into the relationship between density or grain size and SPS parameters, such as green-shaping processing, heating rate, sintering dwell time and sintering temperature. From the results in [8-14], it is clear that the SPS parameter with the major influence on the final grain size is the sintering temperature.

One pending question that has not received attention so far is the kinetics of grain growth during the dwell time after reaching the sintering temperature. As far as we are concerned, grain size versus dwell time determinations in the SPS sintering of α-Al$_2$O$_3$ have been reported by Shen *et al*. [13] only. They only consider two temperatures, namely, 1200 and 1300 ℃. However, these authors do not use their results to measure a diffusion coefficient.

This study is devoted to a rigorous study on the grain growth kinetics during SPS sintering of α-Al$_2$O$_3$. To this purpose, two requisites must be satisfied. First, the range of densities in which grain growth kinetics are dominant over pure densification must be carefully measured. Second, a strict control of the local temperature at the specimen during grain growth must be assured. The first two sections are focused on

these preliminary conditions. The third section reports the grain growth analysis and the value of the diffusion coefficient measured accordingly.

1.2. Experimental

Al_2O_3 powder (Sumitomo Chemical Co., Ltd, Tokyo, Japan) of >99.99% purity, with a particle size of 0.3–0.5 μm and a BET surface area of 5–10 m^2/g, was used as the raw material. The powders were ball-milled in a planetary ball-milling device with tungsten carbide balls. A laser scattering particle analyser (Malvernsizer, Malvern Instruments Ltd, Worcestershire, UK) was used to measure particle sizes. The chemical composition was reanalysed by an X-ray fluorescence spectrometer (XRF, AXIOS, PANalytical, RG ALMELO, Netherlands) to detect any possible contamination. The results allowed us to confirm the degree of purity. No presence of tungsten carbide debris from the balls was detected. SPS was carried out using a SPS device (Dr. Sinter SPS-515S, Fuji Electronic Industrial Co., Ltd., Kanagawa, Japan). The alumina powder was placed in a cylindrical graphite mould with an inner diameter of 15 mm and two graphite punches were set on top and bottom of the graphite die. The amount of powder was set to obtain a 3-mm thick, fully dense sintered body. Graphite sheets were placed between the powder and graphite mould, and punched to avoid direct contact and subsequent damage and to facilitate the removal of the specimen after the test. A thermal insulating carbon felt was placed surrounding the graphite mould to limit the heat radiation loss. The temperature of the graphite mould surface was monitored by an optical pyrometer. The SPS pulse sequence was set to 12:2. Sintering was carried out in a vacuum. The following parameters were studied: (i) sintering temperatures in the range between 1150 and 1400 °C; (ii) sintering dwell times of 1–10 min; (iii) heating rate at 200 °C/min (cooling rate was fixed at 100 °C/min). A uniaxial pressure of 75

32

MPa was applied upon heating and released at the end of the holding time. The density of the samples was measured by the Archimedes method in distilled water. Samples were polished by standard and successive diamond polishing techniques with a grain finish of 1 μm. Polished samples were thermally treated at a temperature of 100 ℃ lower than the sintering temperature for 1 min with a heating rate of 20 °C/min and cooling rate of 10 °C/min in a conventional electric furnace. This condition was chosen because it did not show any difference for the grain size obtained by lower temperature and short time treatment and is effective to reveal the grain boundary clearly than the lower temperature treatment. Scanning electron microscopy (SEM) was carried out on polished and gold coated samples using field-emission SEM (FE-SEM) (HITACHI S5200, Hitachi High-Technologies, Tokyo, Japan) and conventional SEM (PHILIPS XL-30, Philips, Eindhoven, the Netherlands). The equivalent planar diameter *d* was measured from SEM photographs of random locations on the samples, counting more than 300 grains. Statistical analysis was carried out using Origin Pro 8 (Origin Lab, Northampton, US).

1.3. Results and discussion

1.3.1 Relative density at onset of grain growth

The relative densities and mean grain sizes of the sintered specimens obtained at different conditions of sintering temperatures and dwell times for a fixed heating rate of 200 ℃/min, a cooling rate of 100 ℃/min and a pressure of 75 MPa are briefly summarised in Table 1.

TABLE 1

Sintering temperature [°C]	Sintering dwell time [min]	Relative density [%]	Grain size d [μm]	Standard deviation [μm]
	1	78.4	0.188	0.098
	3	89.2	0.230	0.110
1150	5	91.1	0.242	0.137
	10	95.4	0.226	0.096
	1	94.2	0.194	0.107
	3	97.9	0.351	0.163
1200	5	99.6	0.302	0.145
	10	99.0	0.431	0.199
	1	99.8	0.510	0.248
	3	99.9	0.708	0.357
1300	5	100.0	0.581	0.297
	10	100.0	1.010	0.527
	1	100.0	2.202	1.042
	3	100.0	2.169	1.144
1400	5	100.0	2.579	1.284
	10	99.6	5.244	2.722

Table 1: Values of density and grain size of the samples considered in this study. The sintering temperature and dwell time are indicated in the table.

Figure 1 gives a plot of the relative density versus grain size according to the data from Table I. The grain growth started at the last stage of densification, which corresponds to relative density values well above 95%. This suggests that the densification rate was higher than the grain growth rate. Indeed, Lui and DeLo [15] have shown that particle rearrangement by sliding and/or rotation can be active for a large extent for plastically deformable identical spherical particles, up to densities of ~92%. In addition, grain growth was not observed at 1150 °C. At 1200 °C, a relative

density of 94.2% was obtained for a sintering dwell time of 1 min, 97.9 % was obtained for 3 min and dense materials with relative densities above 99.0% were obtained for 5 min or longer. All samples were fully dense at 1300 and 1400 °C with a continuous grain growth evolution with sintering dwell time (Table 1). As a result of this, in-situ grain growth experiments in SPS must be performed in compact powders with an initial density not lower than 97%.
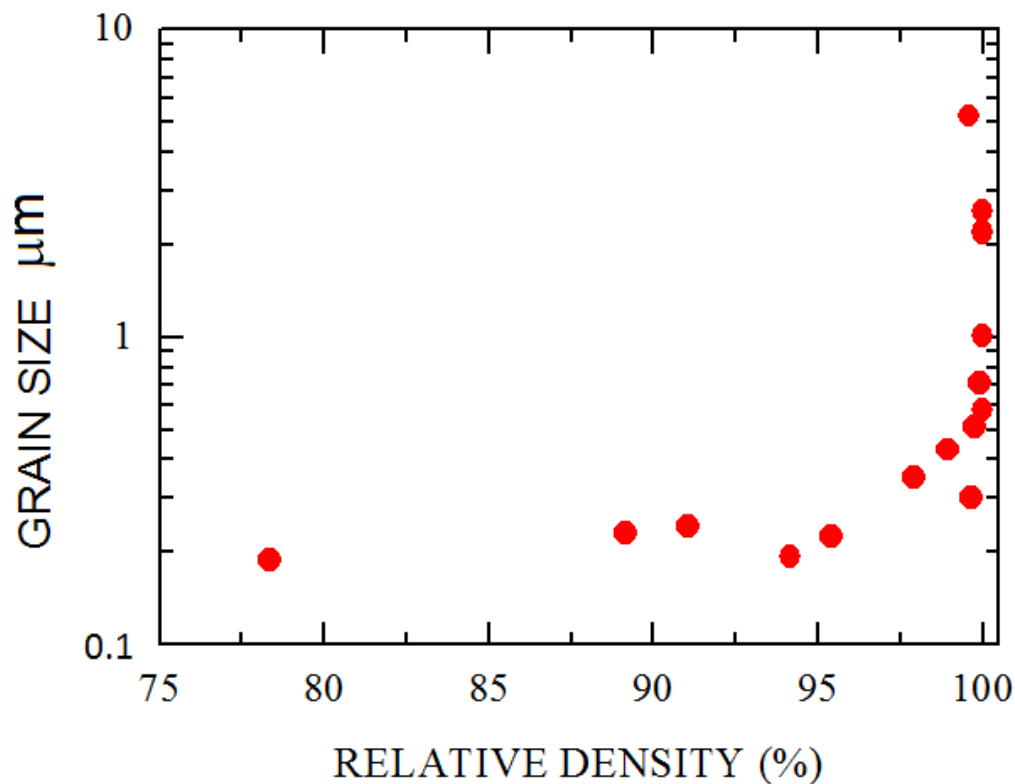
FIGURE 1.1

Figure 1: Grain size versus relative density of all α-alumina specimens from data

displayed in table 1.

The grain size distributions below 1200 °C were mainly Weibull, whereas they were mainly Gumbel over 1300 ºC, which could be related with the last stage of

sintering, when extensive grain growth took place. Recently, phase field simulations have shown that static and dynamic grain growth in ceramic materials are characterised as a Gumbel distribution for grain size [16]. Figure 2 shows a scanning electron micrograph of the grain microstructure. This structure is composed of equiaxial grains with clean interfaces. One remarkable point is the presence of clusters of nanograins and grain coalescence possibly by grain rotation, a fact that has been reported in the literature not only in α-Al_2O_3 prepared by SPS [17], but also in other systems, such as nanocrystalline Y_2O_3 or nano-YAG [18]. This significant microstructural feature is not an artefact of the gold coating, since it was observed even in specimens with no coating.
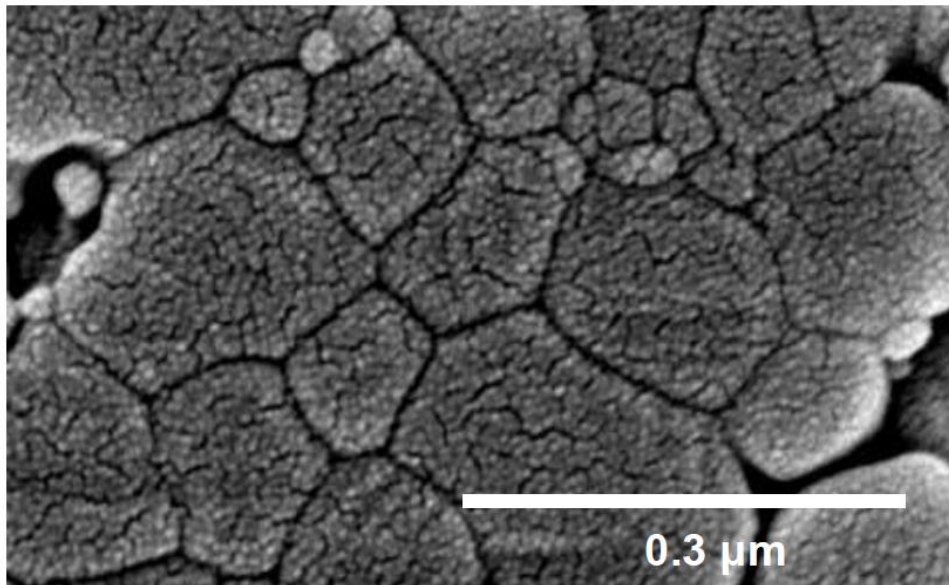
FIGURE 1.2

Figure 1.2: Scanning electron micrograph of the grain microstructure of a sample prepared at 1200ºC during 5 min dwell time.

1.3.2 Local temperature at specimen

Theoretical analysis of the local temperature at the centre of one sample in a SPS furnace has been reported by Moshtaghioun *et al.* [19,20] and applied to the SPS sintering of boron carbide ceramics. These authors showed that the local temperature in the specimen does exceed the temperature at the surface of the graphite mould. They used the heat conduction equation in cylindrical symmetry as follows:

$$\rho C_p \frac{\partial T}{\partial t} - \lambda \nabla^2 T = q \tag{1}$$

where ρ is the density of a material, C_p is the heat capacity of a material, T is temperature, t is time, λ is the heat conductivity of a material and q is heat dissipation per unit volume. From Eq. (1), assuming static heat conditions $\partial T/\partial t = 0$, Moshtaghioun *et al.* [20] derived an equation that can express T_0, the temperature at the sample centre, as a function of T_2, the temperature at the graphite mould surface. To this purpose, they resolved analytically Eq. (1) under the boundary conditions of continuity of temperature at the sample-graphite interface and the continuity of the heat flux (Γ) at that interface, i.e., $\Gamma = -\lambda \frac{\partial T}{\partial r}$. Under these assumptions, the equation determining the temperature at the sample is given by:

$$T_0 - T_2 = \frac{q_1 r_1^2}{4\lambda_1} + \frac{q_2}{4\lambda_2}\left(r_2^2 - r_1^2\right) - \frac{(q_2 - q_1)r_1^2}{2\lambda_2} \ln \frac{r_2}{r_1} \tag{2}$$

where λ_1 is the heat conductivity of the sample, λ_2 is the heat conductivity of graphite, r_1 is the radius of the sample, r_2 is the radius from the centre of the sample to the surface of the mould, q_1 is heat dissipation in the sample and q_2 is heat dissipation in the graphite mould. In the case of alumina, $q_1 \cong 0$ and, therefore, the right side of Eq. (2) is positive. Subsequently, this equation proves that the temperature at the centre of the

37

sample is always higher than the temperature at the surface of the graphite mould. Substituting the present experimental parameters (the heat dissipation in the mould is given by the Joule heating law), $q_2 = \rho_r J^2$, where ρ_r is the resistivity of the graphite mould and J is the electric current density in the mould. Parameters of $q_1 \cong 0$, $\rho_r = 2.54 \times 10^{-5}$ Ωm, $J = 1.0 \times 10^6$ Am^{-2}, $\lambda_2 = 50$ Wm^{-1}K^{-1}, $r_1 = 7.5$ mm and $r_2 = 17.5$ mm give $T_0 - T_2 = 46$ K, which is in good agreement with the results obtained by finite element method modelling [21]. This temperature correction is made in all our grain growth tests.

An aspect which has been ignored so far is the effect of the heating rate on the final grain size. If a constant heating rate is applied, standing by h that heating rate, heat conduction equation can be written as follows:

$$\rho C_p h - \lambda \nabla^2 T = q' \tag{7}$$

Heat dissipation q' equal to the Joule heating $q' = \rho_r J'^2$. We must note that the temperature profile along the graphite die must be the same as measured in static condition (i.e. $h=0$) because the outer temperature of the graphite die is the same as well as the outer heat flow, which is determined by the Stephan-Boltmann's law. In consequence, these two boundary conditions impose the same temperature profile at the graphite die. A comparison of equation (7) with the static condition $-\lambda \nabla^2 T = \rho_r J^2$ gives:

$$J' = \left(J^2 + \frac{\rho C_p h}{\rho_r} \right)^{1/2} \tag{8}$$

This equation shows that the higher the heating rate, the higher the J', which gives a higher value for $T_0 - T_2$. Therefore, the real temperatures of the sample could be much

higher than those recorded with the pyrometer focused on the graphite mold surface. This can be the reason why a higher heating rate resulted in larger grain sizes. This result is displayed in figure 1.3.
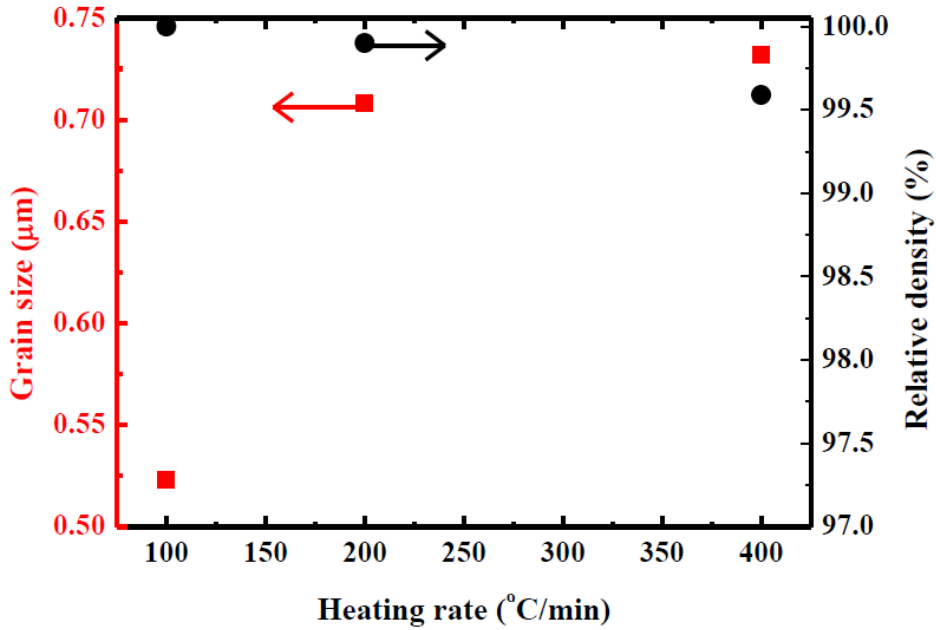
FIGURE 1.3

Figure 1.3: Grain size and relative density versus the heating rate.

1.3.3 Grain growth kinetics

Grain growth kinetics can be analysed by the following general phenomenological equation [22,23]:

$$d^2 - d_0^2 = \Omega \frac{D}{kT} Ft \qquad (3)$$

where t is time, d is grain diameter at time t, d_0 is grain diameter at $t = 0$, D is the grain-boundary diffusion coefficient, k is the Boltzmann constant, T is the temperature, Ω is the volume of the diffusing species and F the driving force per unit area for grain-boundary motion. In pure materials, in which segregation effects are not expected,

39

$F = 2\gamma_{gb}/\delta_{gb}$ with γ_{gb} the interfacial energy of the grain boundaries and δ_{gb} their thickness.

The values of the average grain size versus the time after reaching the sintering temperature at different temperatures (1200, 1300 and 1400 ºC) in alumina specimens annealed in a SPS furnace were recorded. Using these data and the parameters of $\delta_{gb} \cong 1.0 \times 10^{-9}$ m, $\gamma_{gb} \cong 0.1$ J/m^2 and $\Omega \cong 1.22 \times 10^{-29}$ m^3, the grain-boundary diffusion can be determined [24]. The activation energy for grain boundary diffusion (Q_{gb}) is found to be 350 ± 50 kJ/mol and the pre-exponential constant D_0 of 1.6×10^{-3} m^2/s.
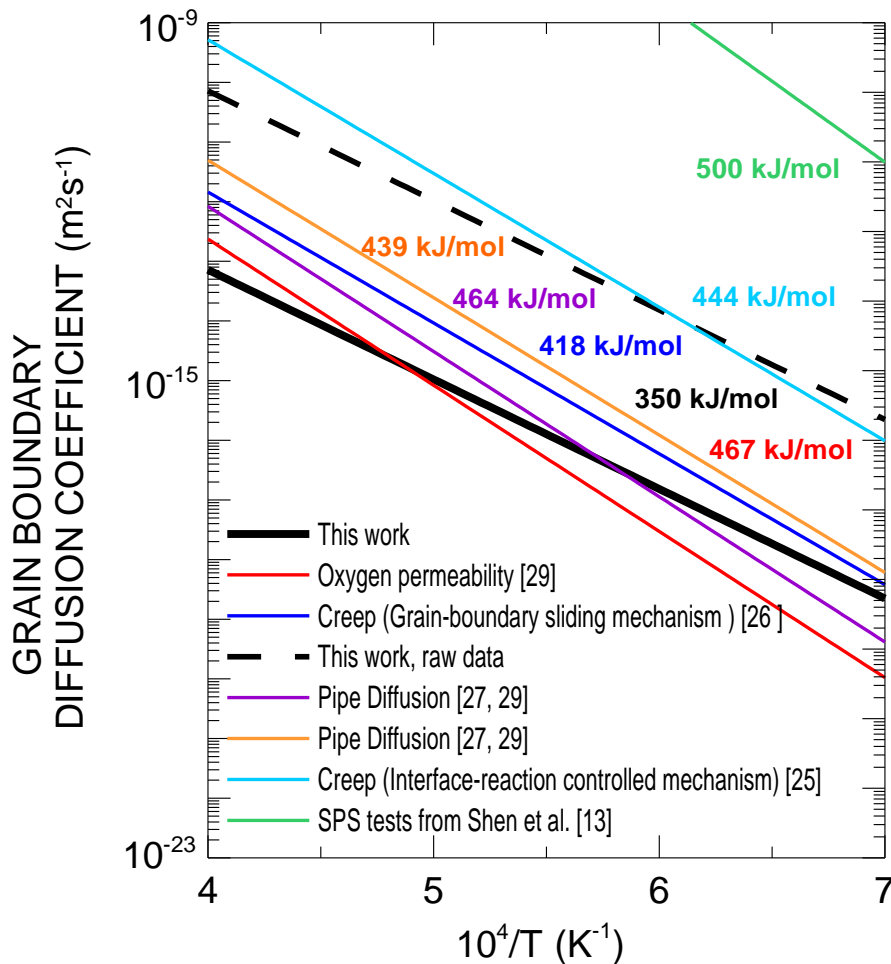
FIGURE 1.4

Figure 1.4: Grain boundary diffusion coefficient in alumina versus the reciprocal temperature. Raw data are provided (as obtained from grain-growth determinations during SPS annealing) as well as the expected diffusion coefficient.

40

The comparison with data in the literature should be considered with caution. Firstly, the number of reported data of diffusion coefficients in alumina is high, with a considerable scattering depending on either the diffusion path, the diffusing species or the experimental technique used for measurements. Secondly, the grain motion needs the transport of both alumina cations and oxygen anions. In alumina, oxygen anions are by far the slowest diffusing species. Therefore, they control the whole process of mass transport [25–29]. Thirdly, it is reasonable to think that most of the mass transport for grain motion takes place along the grain boundaries, i.e., grain growth is controlled by the grain-boundary diffusion of oxygen.

As a consequence, we will restrict ourselves to a comparison of our diffusion coefficient with reported values of oxygen diffusion along the grain boundaries. Figure 3 displays the temperature dependence of the grain-boundary diffusion of oxygen in alumina. Our experimental results are plotted as a dashed black line.

The reported results for the grain-boundary diffusion coefficient measured by oxygen permeability tests [29], high temperature creep experiments [25,26] and pipe diffusion [27,29] are also plotted. Finally, we calculated the diffusion coefficient that should be expected from the results of Shen *et al.* [13] for SPS sintering in coarse-grained alumina powders.

Several discrepancies must be discussed. First, the results of Shen *et al.* are compatible with a diffusion coefficient that is much larger than those reported previously in the literature, including ours. The activation energy derived from their results is 500±30 kJ/mol. Such energy is also much higher than those previously published (provided in the plot). At this point, we can only speculate on the origin of such a large difference. It might be related to the fact that the initial density of the powder compacts in their grain growth tests was much lower than 97% and some

densification could be occurring simultaneously and also they provide grain growth data at two temperatures (1200 and 1300 ℃) only.

Secondly, if we focus on a comparison of our results with those published previously, at first sight it is possible to realise that our diffusion coefficient is larger than all of them except one, namely the creep diffusion coefficient reported by Cannon *et al.* assuming interface-controlled creep [25]. Such a coefficient was revised by Heuer et al. [26] in the case of a grain-boundary sliding mechanism for creep. In general, our results are systematically much higher (close to three orders of magnitude) than those of pipe diffusion, creep or oxygen permeability-based ones (Fig. 3). A possible explanation for this is proposed now and it is based on the recent discovery reported by Heuer et al. [28] in the literature of diffusion in α-Al_2O_3. These authors claim that grain-boundary diffusion in this material is controlled by the collective motion of disconnections, i.e., boundary ledge defects characterised by a step length h and a Burgers vectors b. Grain-boundary diffusion is ruled by the glide of these defects. The mechanism of such motion demands the diffusion of alumina and oxygen vacancies to assure electroneutrality, meaning that individual disconnections acquire some charge during motion [28]. Bearing this idea in mind, Eq. (3) needs updating. Indeed, during spark plasma sintering, an electric voltage is applied through the sample (~10 V). The electric field associated to this voltage induces a force per unit area (i.e. force on the disconnections) that must be added to Eq. (3). Such force, ignored until now, accounts for the high values of the grain-boundary diffusion coefficient when determined through SPS experiments.

The proposed modification in Eq. (3) gives rise to the following law:

$$d^2 - d_0^2 = \Omega \frac{D}{kT}\left(2\frac{\gamma_{gb}}{\delta_{gb}} + \frac{n_D q \phi}{h d^2} \right)t \qquad (4)$$

42

FIGURE 1.5

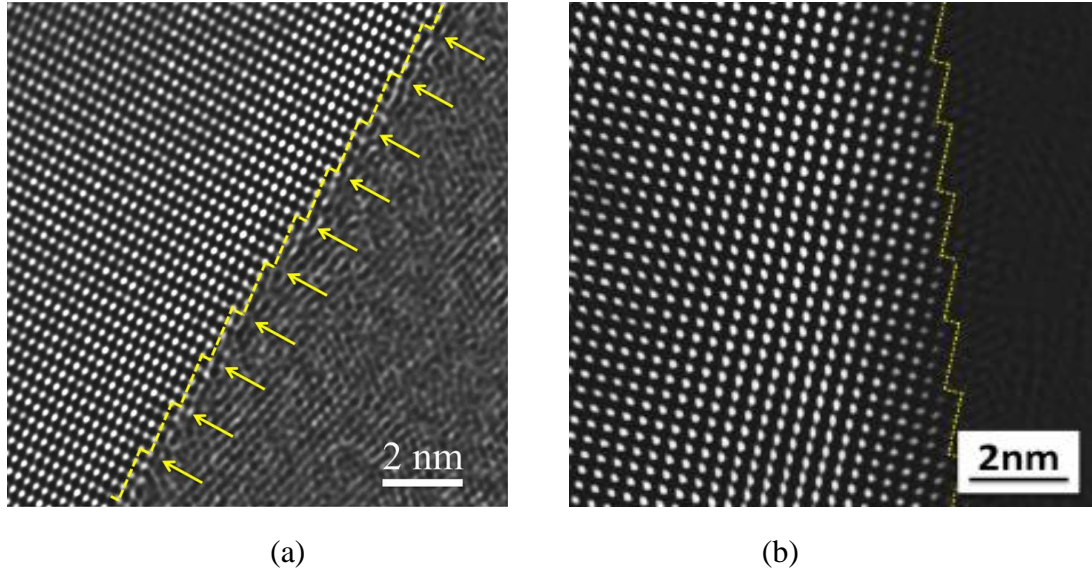(a)   (b)

Figure 1.5: HRTEM micrographs of disconnections as shown in references [28] (a) and [29] (b). Reproduction under permission.

In this equation, $\phi \sim 10$ V is the electric potential, n_D is the number of disconnections in one grain and q is the electric charge of the disconnection. The number of disconnections per grain is determined from microstructural observations reported in [28], which display an average distance $l \sim 2$ nm between disconnections. Therefore, a good estimate of n_D would be $n_D \approx d/l$. The electric charge is also estimated from the mechanism proposed by Heuer *et al.* [28] for the motion of disconnections. The collective motion demands at least one alumina vacancy per unit cell electrically compensated with oxygen vacancies accordingly. Therefore, since the area of a disconnection is $\sim hd$, the electric charge would be given by $\sim 3ehd/a^2$, where *a*

is the lattice parameter and e the electron charge. A quantitative analysis of the two driving forces for grain-boundary motion shows that the first one, i.e., the contribution of curvature only, $F_1 = 2\gamma_{gb}/\delta_{gb}$, is $\sim 2\times 10^8$ Nm^{-2}. Alternatively, the contribution of the electric potential applied to the specimen during SPS, which is given by $F_2 = \dfrac{n_D q\phi}{hd^2} \approx 3\dfrac{e\phi}{\lambda a^2}$, is approximately equal to 2×10^{11} Nm^{-2}. It is important to note that the fact that the disconnection-based driving force does not depend on the grain size, i.e., it affects all grains simultaneously. Thus, it does not alter the grain size distribution during grain growth. Numerical values estimated above show that the F_2 driving force is three orders of magnitude larger than the usual curvature induced one, F_1. If F_2 is ignored, the diffusion coefficient is artificially overestimated by these three orders of magnitude. This is what must be happening with the SPS grain growth derived diffusion coefficient when no attention is paid to the effect of the electric field on disconnections.

Figure 3 shows also the corrected value of the diffusion coefficient (black solid line). The agreement with the reported data is excellent within one order of magnitude and half, the typical scattering range of this quantity. It is particularly consistent with the pipe diffusion coefficient values. One reason for this could be the special microstructure of this material, composed of nanoclusters, which release many potential diffusion paths which can be described as grain-boundary dislocations.

Finally, regarding the activation energy values [27,29], our SPS data are lower than those reported previously in the literature. The average value of these previously published activation energies is Q = 446±30 kJ/mol, whereas our SPS tests give rise to Q = 350±50 kJ/mol, which is significantly smaller. At present, we cannot explain such a difference because many factors can account for this fact. One of them could be the possible presence of different types of impurities in the set of different alumina polycrystals under comparison. Given the highly stoichiometric character of this

44

compound, even tiny amounts of impurity defects can induce changes on the transport coefficients. Future works on this topic would be required to refine the values of the activation energy in alumina and give a more accurate estimate of this quantity.

1.4. Conclusions and scientific achievements.

Grain growth tests during SPS annealing have been carried out. The initial conditions for a proper analysis, i.e., initial density and local temperature at the powder compacts, have been determined. Grain growth tests at different temperature have permitted to obtain a grain-boundary diffusion coefficient. This first value overestimates the real value of this quantity, because the local electrodynamical effects of the electric current on the preexistent disconnections are ignored. A quantitative law for correct analysis of grain growth data under SPS annealing is proposed. According to this law, the grain-boundary diffusion coefficient is given by $D = 1.6 \times 10^{-6} exp(-350 (kJ/mol)/RT)$ $m^2 s^{-1}$. This value is in reasonable agreement with those proposed previously from high temperature creep analysis or oxygen permeability studies. It is especially in good agreement with those proposed for pipe diffusion. This fact is consistent with the existence of many pipe diffusion paths on the microstructure of the dense specimens.

References

[1] A Okada, Automotive and industrial applications of structural ceramics in Japan. J. Eur. Ceram. Soc. 28 (2008)1097-104.

[2] A Krell, P Blank, H Ma, T Hutzler, M Nebelung, Processing of High-Density Sub micrometer Al_2O_3 for New Applications. J. Am. Ceram. Soc. 86 (2003) 546–53.

[3] A Krell. A new look at the influences of load, grain size, and grain boundaries on the room temperature hardness of ceramics. Int. J Refract. Met. Hard Mater. 16 (1998) 331-5.

[4] J Fang, AM Thompson, MP Harmer, HM Chan, Effect of Yttrium and Lanthanum on the Final-Stage Sintering Behavior of Ultrahigh-Purity Alumina. J. Am. Ceram. Soc. 80 (1997) 2005–2012.

[5] M Tokita. Trends in Advanced SPS Spark Plasma Sintering System and Technology. J. Soc. Powder Technol. Japan. 30 (1993) 790–804.

[6] EA Olevsky, WL Bradbury, CD Haines, DG Martin, D Kapoor D, Fundamental Aspects of Spark Plasma Sintering: I. Experimental Analysis of Scalability. J. Am. Ceram. Sci. 95 (2012) 2406-13.

[7] M Demuynck, JP Erauw, O Van der Biest, F Delannay, F Cambier. Densification of alumina by SPS and HP: A comparative study. J. Eur. Ceram. Soc. 32 (2012) 1957-64.

[8] F Meng, F Zhang, W Huang, W Yang, M Guo, X Jiang, Z Tian. Fabrication of ultrafine-grained alumina ceramics by two different fast sintering methods. Ceram. Inter. 37 (2011) 1973–7.

[9] J Gurt Santanach, A Weibel, C Estournès, Q Yang, C Laurent, A Peigney, Spark plasma sintering of alumina: Study of parameters, formal sintering analysis and hypotheses on the mechanism(s) involved in densification and grain growth. Acta Mater. 59 (2011) 1400-8.

[10] Y Aman, V Garnier, E Djurado. Spark plasma sintering kinetics of pure α-alumina. J. Am. Ceram. Soc. 94.(2011) 2825-33.

[11] Y Aman, V Garnier, E Djurado, A Screening Design Approach for the Understanding of Spark Plasma Sintering Parameters: A Case of Translucent Polycrystalline Undoped Alumina. J. Appl. Ceram. Technol. 7 (2010) 574–86.

[12] BN Kim, K Hiraga, K Morita, H Yoshida. Effects of heating rate on microstructure and transparency of spark-plasma-sintered alumina. J. Eur. Ceram. Soc. 29 (2009) 323-7.

[13] Z Shen, M Johnsson, Z Zhao, M Nygren, Spark plasma sintering of alumina. J. Am. Ceram. Soc. 85 (2002) 1921–7.

[14] ZA Munir, U Anselmi-Tamburini, M Ohyanagi, The effect of electric field and pressure on the synthesis and consolidation of materials: A review on the spark-plasma sintering method. J. Mater. Sci. 41 (2006) 763-777.

 [15] JX Lui, DP DELo. Particle rearrangement during powder compaction. Metall. Mater. Trans. A. 32A (2001) 3117-3124.

[16] BM Moshtaghioun, D Gomez-Garcia, FL Cumbrera-Hernandez, A Dominguez-Rodriguez. A phase-field model of 2D grain size distribution in ceramics. J. Eur. Ceram. Soc. 34 (2014) 2731-2736.

[17] A. Morales, R. Poyato. A. Gallardo, A. Munoz, A. Domínguez-Rodríguez. Evidence of nanograin cluster coalescence in spark plasma sintered α-Al_2O_3. Scripta mater. 69 (2013) 529-532.

[18] R. Chaim, R. Marder, C. Estournès, Z. Shen. Densification and preservation of ceramic nanocrystalline character by spark plasma sintering. Adv. Appl. Ceram. 111 (2012) 280-285.

47

[19] BM Moshtaghioun, FL Cumbrera, AL Ortiz, M Castillo-Rodríguez, D Gómez-García, Additive-free superhard B_4C with ultrafine-grained dense microstructures. J. Eur. Ceram. Soc. 34 (2014) 841-8.

[20] BM Moshtaghioun, FL Cumbrera-Hernández, D Gómez-García, S de Bernardi-Martín, A Domínguez-Rodríguez, A Monshi, MH Abbasi MH. Effect of spark plasma sintering parameters on microstructure and room-temperature hardness and toughness of fine-grained boron carbide (B_4C). J. Eur. Ceram. Soc. 33 (2013) 361–9.

[21] U Anselmi-Tamburini, S Gennari, JE Garay, ZA Munir, Fundamental investigations on the spark plasma sintering/synthesis process II. Modeling of current and temperature distributions. Mater Sci Eng A 394 (2005) 139-148.

[22] MN Rahaman, Ceramic processing and sintering. Marcel Dekker Inc., New York, US (1995) pp 428-30.

[23] R Chaim, Activation energy and grain growth in nanocrystalline Y-TZP ceramics. Mater. Sci. Eng. A 486 (2008) 439-446.

[24] E Dorre, H Hubner: Alumina, Springer-Verlag, Berlin (1984) pp. 41-49.

[25] RM Cannon, WH Rhodes, AH Heuer, Plastic deformation of fine-grained alumina (Al_2O_3): I. Interface-controlled diffusional creep, J. Am. Ceram. Soc. 63 (1980) 46-53.

[26] AH Heuer, NJ Tighe, RM Cannon, Plastic deformation in fine-grained alumina (Al_2O_3): II. Basal slip and non-accommodated grain-boundary sliding. J. Am. Ceram. Soc. 63 (1980) 53-58.

[27] AH Heuer. Oxygen and aluminum diffusion in α-Al_2O_3: How much do we really understand? J. Eur. Ceram. Soc. 28 (2008)1495-507.

[28] AH Heuer, MZ Azar, A disconnection mechanism of enhanced grain boundary diffusion in Al_2O_3. Scripta mater. 102 (2015) 15-18.

[29] AH Heuer, MZ Azar, H Guhl, M Foulkes, B Gleeson, T Nakagawa, Y Ikuhara, W Finnis. The band structure of polycrystalline Al_2O_3 and its influence on transport phenomena. J. Am. Ceram. Soc. 99 [3] (2016) 733-747.

Chapter 2

Sintering of alumina-whisker-reinforced alumina composites. General conditions. Microstructural characterization. Room-temperature fracture properties.

Summary

Densification of alumina whisker-reinforced alumina ceramics by spark plasma sintering (SPS) has been investigated with the aim of obtaining a fine-grained microstructure and also studying the effect of whisker addition on the room-temperature mechanical properties. It was found that whisker addition retards slightly the sinterability of alumina by whisker hindering of particle rearrangement. Besides, the internal stress on the alumina matrix particles reduced due to the presence of a whisker network structure of strong rigid boundaries. Nevertheless, near fully-dense and fine-grained alumina ceramics with alumina whisker content between 3wt% and 10wt% could be obtained under appropriate SPS conditions. The hardness of alumina ceramics with 3wt% was comparable to that of pure alumina ceramics (~26GPa) whereas its fracture toughness (5.6 MPa m$^{1/2}$) was higher (4.2 MPa m$^{1/2}$). Crack bridging by well-dispersed whiskers and whiskers pull-out were identified as the main toughening mechanisms.

2.1-Introduction

As commented in the prologue of this dissertation book, alumina ceramics have attracted the highest investment as structural ceramics due to its excellent chemical stability, good mechanical properties and oxidation resistance together with a low production cost. However, its intrinsic low fracture toughness is a limiting factor for a broader application range [1-3]. It is well known that the microstructural refinement by advanced sintering techniques like spark plasma sintering (SPS) can improve their strength, hardness and to some extent fracture toughness [4-8]. Another efficient approach to this goal is the microstructural reinforcement by addition of secondary phases [9-24]. Accordingly, several secondary phases, either particles or whiskers/fibers, such as SiC particles $-$ Al_2O_3 [9-11], SiC whiskers $-$ Al_2O_3 [12], TaC whiskers $-$ Al_2O_3 [13], carbon nano tubes (CNT) $-$ Al_2O_3 [14-21], BN $-$ Al_2O_3 [22, 23], metal $-$ Al_2O_3 [24] have been used to fabricate alumina-based composites. It is reported that the addition of SiC particles or SiC whiskers to Al_2O_3 matrix enhances hardness and fracture toughness by changing the fracture mode from intergranular in pure alumina polycrystals to mixed intergranular-transgranular mode in alumina-based composites [10-12]. Moreover, the recent studies have shown that the carbon nanotubes are also efficient additives to the aim of improving fracture toughness and flexure strength of Al_2O_3 ceramics whereas the hardness is generally reduced [17-21].

In many high-temperature structural applications, alumina-based composites with high oxidation resistance are required. This is the main drawback of the non-oxide secondary phases (SiC, CNT, or metals): their mechanical properties degradation at elevated temperatures under air [3,23]. Furthermore, the bonding character between alumina grains and second phases in alumina-based composites like CNT/ Al_2O_3 ceramics [17] is not still clear and depends strongly on the processing procedure.

52

Indeed, the bonding character can affect mechanical properties relevantly [17]. The improved fracture toughness of SiC whiskers-reinforced Al_2O_3 ceramics [10-12] or CNT-reinforced ones [17-21] confirm that whiskers are promising candidates for Al_2O_3 ceramics reinforcement. In order to overcome the drawback of non-oxide additives, an appropriate alternative is the use of Al_2O_3 whiskers/fibers, that obviously cannot oxidize and do not have bonding incompatibility with the matrix. Surprisingly, the reinforcement of Al_2O_3 ceramics with Al_2O_3 whiskers has not been studied previously. Fortunately, Al_2O_3 whiskers produced by vapor-liquid-solid deposition (VLS) techniques [25,26], are available at industry level at competitive cost. In addition to this, Al_2O_3 has previously been compacted successfully by spark plasma sintering (SPS) and the systematic study of SPS sintering conditions with limited grain growth and higher hardness values has been reported before [4-8]. Therefore it seems quite reasonable to get advantage of the SPS technique to prepare whiskers-reinforced alumina ceramics with enhanced mechanical properties. This is the objective of this study, which is aimed at investigating the effect of the additions of Al_2O_3 whiskers on the sinterability and room-temperature mechanical properties of SPSed alumina composites.

2.2- Experimental procedure

Al_2O_3 powders (Sumitomo Chemical Co., Ltd, Tokyo, Japan) of > 99.99 % purity, with particle size $0.3 - 0.5$ μm and BET surface area $5 - 10$ m^2/g and Al_2O_3 whisker (Neoker, S. L., Milladoiro, Spain) of > 5 μm in length and with aspect ratio 3:1 were used as raw materials. Three powder batches were prepared with different compositions, one of which contains only Al_2O_3 powders, while other ones are Al_2O_3 powders with 3wt% and 10 wt% Al_2O_3 whiskers, respectively. Hereafter, the pure Al_2O_3

sample is labelled as AW00, the composite with 3 wt% whiskers as AW03, and consequently the 10 wt%-whiskers composite as AW10. The powder mixtures were subjected to ball-milling with Si_3N_4 balls for 24 h in ethanol. Later on, the resulting slurry was dried on a hot plate in air.

Subsequently, the as-received Al_2O_3 powders and the ball-milled powder mixtures of with 3wt% and 10 wt% Al_2O_3 whiskers were densified by SPS (Dr. Sinter SPS-515S, Fuji Electronic Industrial Co., Ltd., Kanagawa, Japan), using a graphite mold with inner diameter of 15 mm. The amount of powders was set to obtain a 3 mm thick of fully dense sintered body. A thermal insulating carbon foil was placed surrounding the graphite mold to limit the heat loss. Temperature of the graphite mold surface was monitored by an optical pyrometer and the SPS pulse sequence was set to 12:2. SPS was carried out in dynamic vacuum (i.e.,~6Pa) and the following parameters were studied: (i) sintering temperature, in the range 1150-1400 °C and (ii) sintering dwell time, in the range 1-10 min. In all cases, the SPS was performed under uniaxial mechanical pressure of 75 MPa (applied during the whole sintering process, including heating and cooling ramps) with heating rate set at 200 ºC/min and cooling rate of 100 ºC/min.

The relative density of the samples was measured by the Archimedes method in distilled water as the immersion media. The microstructural characterization was carried out by scanning electron microscopy (FE-SEM; HITACHI S5200, Hitachi High-Technologies, Tokyo, Japan). SEM observations were done on fracture surfaces and on polished-gold-coated surfaces polished to a 1 μm-finish using conventional ceramographic methods. The polished surfaces were thermally etched at 1150 °C for one minute dwell time with a heating rate of 20 °C/min and cooling rate of 10 °C/min.

The equivalent planar diameter *d* was measured from SEM photographs, counting more than 380 grains.

In order to study the compaction behavior during SPS, the following experiment was performed: one SPS test at 1300 °C in the same graphite mold used previously with constant pressure of 27 MPa applied during heating (minimum contact pressure for safety reasons) up to 1300 °C. Then, the temperature was held for one minute to ensure thermal stability. Later on, while keeping this temperature, pressure was increased up to 100 MPa and then it was relieved. Temperature, pressure and powder shrinkage were monitored. The length from the top to the bottom of punches was measured after the die cooled down to room temperature and the sample thickness was calculated considering the length of the two punches used. Additionally, a blank test was also carried out by setting die, punches and graphite sheet without sample powder following the same procedure mentioned above. By means of this blank test, the effect of thermal expansion and elastic deformation of the graphite elements can be calibrated.

The hardness (H_v) and fracture toughness (K_{IC}) of the selected specimens were measured by Vickers indentation tests on polished samples using a Vickers indentation tester (Struers A/S, DK-2750 Bullerup, Denmark) equipped with a diamond Vickers indenter, under a load of 9.8 N and dwell time of 10 s. At least 10 measurements per specimen were recorded to average the hardness and the fracture toughness. The hardness and toughness were determined using the standard expressions $H_v=2P/a^2$ and $K_{IC}=0.016(E/Hv)^{0.5}Pc^{-1.5}$[27,28] where *a* and *c* are the length of the diagonal of the residual impression and the semi-length of the surface trace of the radial cracks measured by optical microscopy, respectively, and *E, P* the Young modulus and indentation load, respectively.

55

2.3. Results

2.3.1. Sintering behavior

Results of relative density, mean grain size, and grain size distribution of sintered bodies obtained at different SPS conditions are summarized in Table 1. Both the relative density and grain size evolution as a function of sintering dwell time are plotted in Fig. 1(a) and Fig. 1(b), respectively for the test at 1300 ºC. Additionally, the evolution of the relative density and grain size with SPS temperature for 3 minutes of SPS dwell time is shown in Fig. 1(c) and Fig. 1(d), respectively.

Table 1

Composition	Sintering temperature (°C)	Dwell time (min)	Relative density (%)	Grain size d (μm)	Standard deviation (μm)
AW00 (Alumina powder 100%)	1150	10	95.4	0.226	0.096
	1200	3	97.9	0.351	0.163
	1300	1	99.8	0.510	0.248
		3	99.9	0.581	0.357
		5	100.0	0.708	0.297
		10	100.0	1.010	0.527
	1400	3	100.0	2.169	1.144
AW03 (Whisker 3 mass%)	1200	3	90.4	0.282	0.118
	1300	1	97.2	0.441	0.222
		3	99.0	0.446	0.244
		5	99.9	0.739	0.494
	1400	3	99.5	0.772	0.281
AW10 (Whisker 10 mass%)	1200	3	90.2	0.216	0.169
	1300	1	93.8	0.307	0.158
		3	95.5	0.306	0.159
		5	95.9	0.304	0.185
		10	95.8	0.325	0.186
	1400	3	96.9	0.440	0.252

Table 1. Processing conditions and microstructural features of the AW00, AW03 and AW10 alumina-based ceramics by SPS.
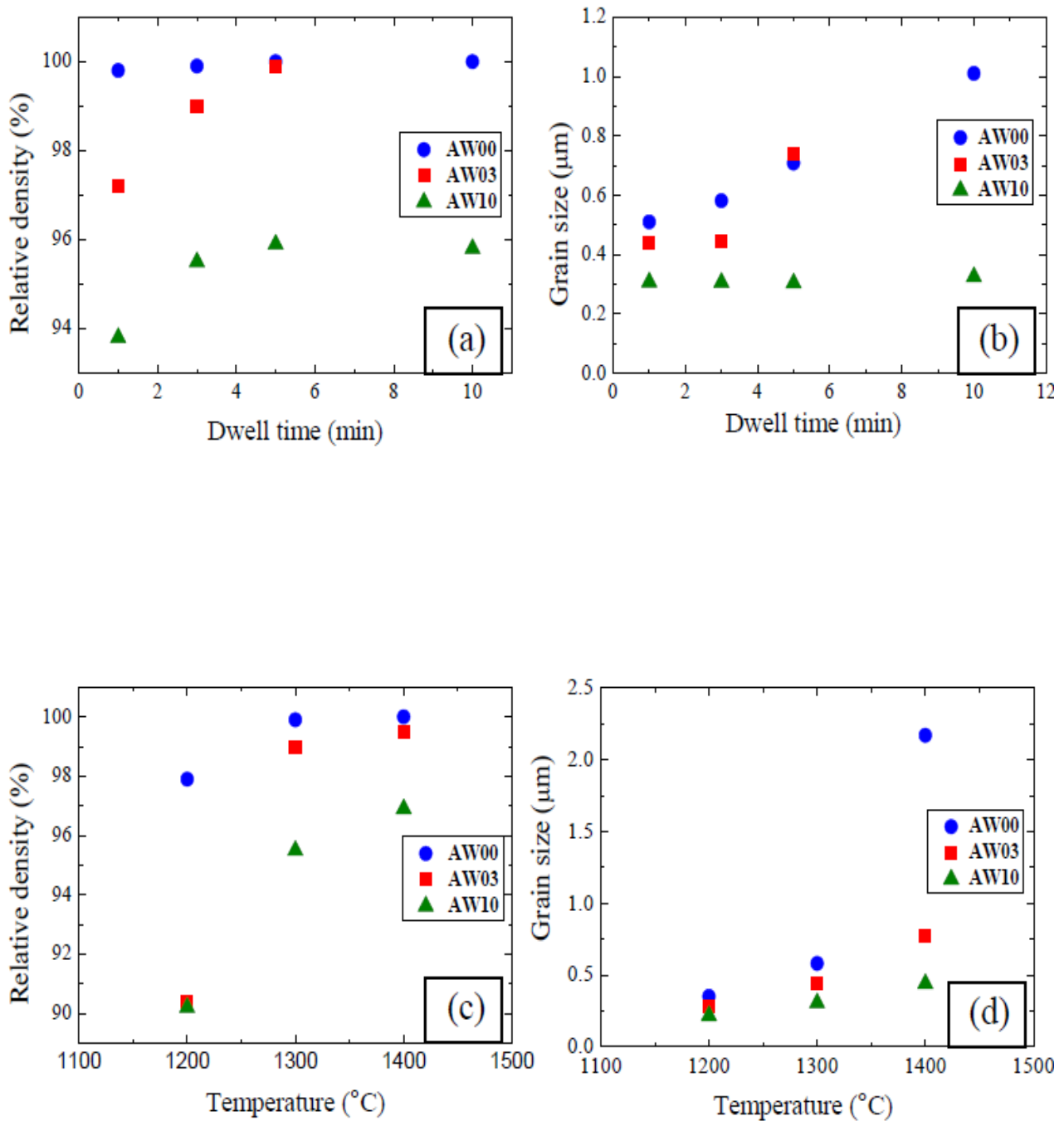
57

FiGURE 2.1

Fig. 2.1. Plot of (a) relative density and (b) grain size as a function of sintering dwell time at 1300 °C, as well as (c) relative density and (d) grain size as a function of sintering temperature for 3 min dwell.

A heating rate of 200 ℃/min, cooling rate of 100 ℃/min and pressure of 75 MPa were applied for these SPS experiments. As it is shown in Fig. 1(a) and Fig. 1(c), near fully-dense AW00 specimens (relative density higher than 98%) was obtained at SPS temperatures higher than 1200 ℃ for any dwell time, while grain size increases with dwell time and remarkably with sintering temperature. It can be concluded that the optimal SPS conditions for the pure alumina powders are 1300 ℃ for 1-3 min with near fully-dense specimen and limited grain size of 0.5-0.6 μm. When whiskers are added, it is clear from Fig. 1(a) and Fig. 1(c), that 3wt% whiskers addition retards densification slightly compared to pure alumina at the same SPS conditions while it limits grain growth strongly. In the case of higher whisker addition (10wt%), the densification inhibition (Fig. 1(a) and Fig. 1(c)) is more relevant and grain growth is hindered effectively and decreases to much lower values than those of as-received and 3wt% whiskers-added under identical SPS conditions (Fig. 1(b) and Fig. 1(d)). It is especially remarkable the grain size evolution of AW10 at 1300 ℃, which remains constant (0.3 μm) whatever the sintering dwell time value. Moreover, grain growth was hardly observed at 1400 ℃ in AW10. Therefore, it seems that Al_2O_3 whiskers addition promotes microstructure refinement and stability. On the other hand, the higher the SPS temperature, the higher the grain size difference between AW00 and Al_2O_3 whisker-reinforced Al_2O_3 matrix ceramics (AW03 and AW10). For example, the grain size after sintering at 1400 ℃ with a dwell time of 3 min of AW00 was 2.17 μm, whereas it was ~0.77 μm and ~0.44 μm for AW03 and AW10 under the same sintering conditions, respectively. Proper SPS conditions to achieve a fine microstructure of 0.45 μm grain size with a relative density ∼ 99 % is 1300 ℃–75MPa–3 min for AW03. Under identical SPS conditions for AW10, significant microstructural refinement to 0.3 μm was observed while relative density is around 95.5%. Indeed, it became evident from Fig. 1

that for AW10 ceramics, SPS conditions of 1400 ºC-3min are the best compromise to the goal of higher densification (~97%) together with the retention of ultrafine grains (0.44 μm).

2.3.2. Microstructural characterization

SEM images of polished cross-sections of AW00, AW03 and AW10 sintered under SPS at 1300 ºC for 1 min are shown in Fig. 2(a), Fig. 2(b) and Fig. 2(c), which are characterized by densities of 99.8%, 97.2% and 93.8%, respectively. A fully dense matrix was observed in all three ceramics (Fig. 2(a), Fig. 2(b) and Fig. 2(c)), while some residual porosity is observed in the whiskers-matrix interface in AW03 and AW10 specimens (Fig. 2 (b) and Fig. 2(c) insets, red arrows point out the cross-section of a whisker). The higher the Al_2O_3 whiskers content, the higher the porosity and the weaker whisker-matrix interface is found. Therefore, the Al_2O_3 whiskers, which are expected to be accommodated deficiently during SPS, retard the sinterability of alumina by partially blocking the alumina particles rearrangement and therefore some porosity could be observed in their vicinity. Besides, Fig. 2(a), Fig. 2(b) and Fig. 2(c) show that a higher whiskers content is increasingly effective in retaining a fine-grained microstructure.

SEM image of the fracture surfaces of a AW03 specimen sintered under SPS at 1300 ºC for 1 min and a AW10 specimen sintered under SPS at 1400 ºC for 3 min is shown in figure 3a and b, respectively.
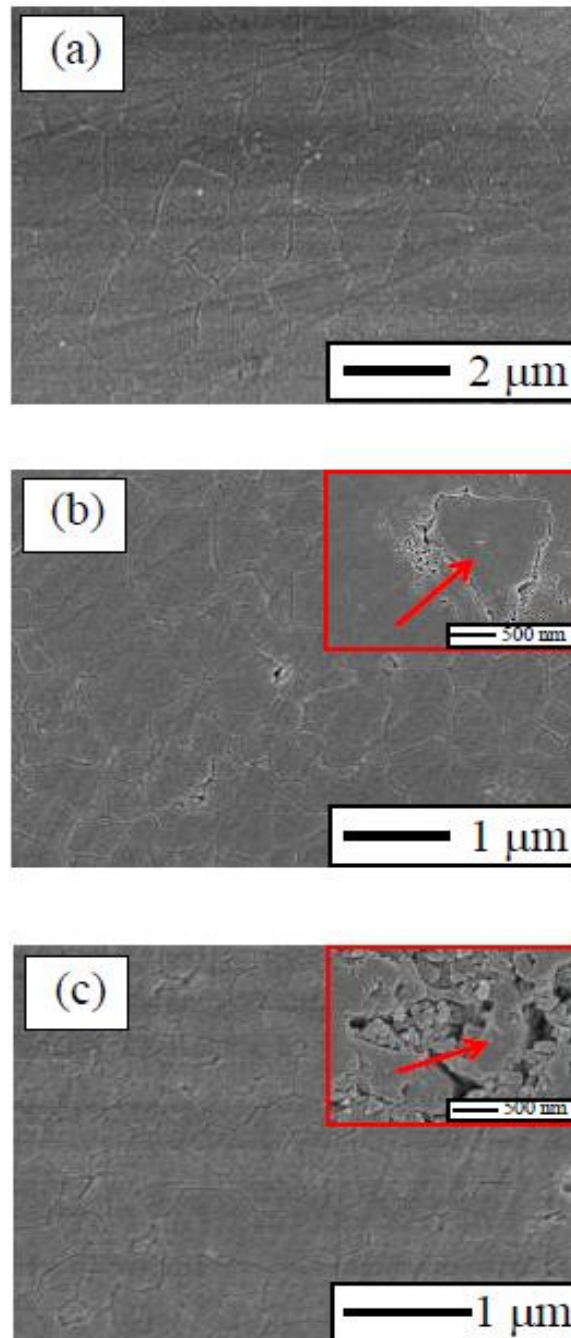
FIGURE 2.2

Fig. 2.2. Polished-surface SEM micrographs of (a) AW00, (b) AW03 and (c) AW10 SPSed at 1300 °C for 3 min with heating rate of 200 °C/min, cooling rate of 100 °C/ min and pressure of 75MPa. The insets indicate the cross-section of a whisker and the presence of porosity in its vicinity.
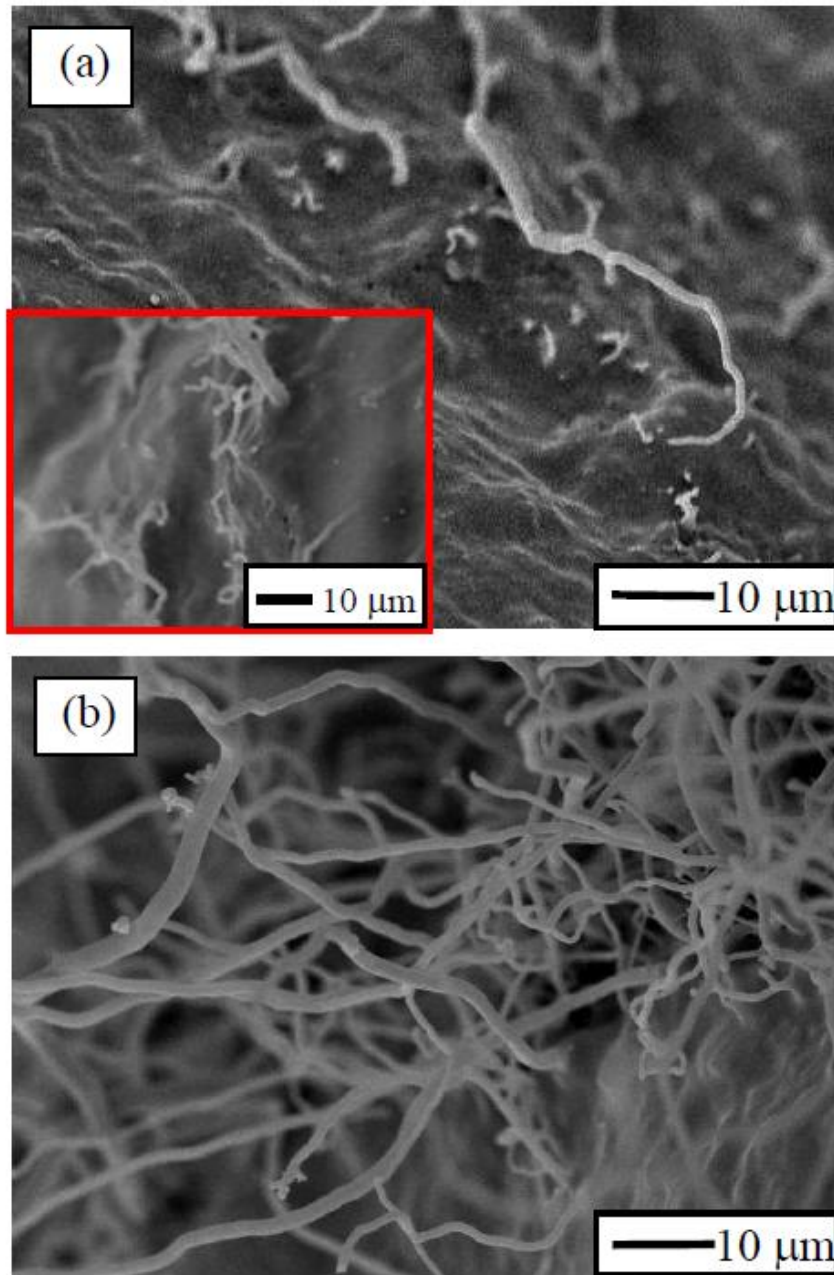
FIGURE 2.3

Fig. 2.3. SEM micrographs of the fracture surfaces of the broken (a) AW03 sintered at 1300 °C for 1 min and (b) AW10 sintered at 1400 °C for 3 min with heating rate of 200 °C/min, cooling rate of 100 °C/ min, and pressure of 75MPa.

Considering that there is the presence of porosity in the vicinity of alumina whiskers as shown in Fig. 2(b) and Fig. 2(c) insets, it results in the weakening of

whisker-matrix interfaces and plays a role as an effective toughening mechanism by whisker bridging at the wake of the crack tip by alumina whiskers. In fact, the inset in Fig. 3a shows some Al_2O_3 whiskers emerging from the fracture surface because of a well-dispersion of them in the alumina matrix. Such homogeneous dispersion contributes to bridge the crack and the later fiber pull out. On the contrary, whisker accumulation in AW10 specimen reduces the effective role of fibers to activate these toughening mechanisms as it can be seen in Fig. 3b.

3.3. Compaction behavior of powders

Compaction behavior of powders or powder shrinkage under spark plasma sintering is studied through the plot of sample thickness as a function of SPS pressure from 27 MPa to 100 MPa and its unloading at a constant SPS temperature of 1300 ºC which is provided in Fig. 2.4.
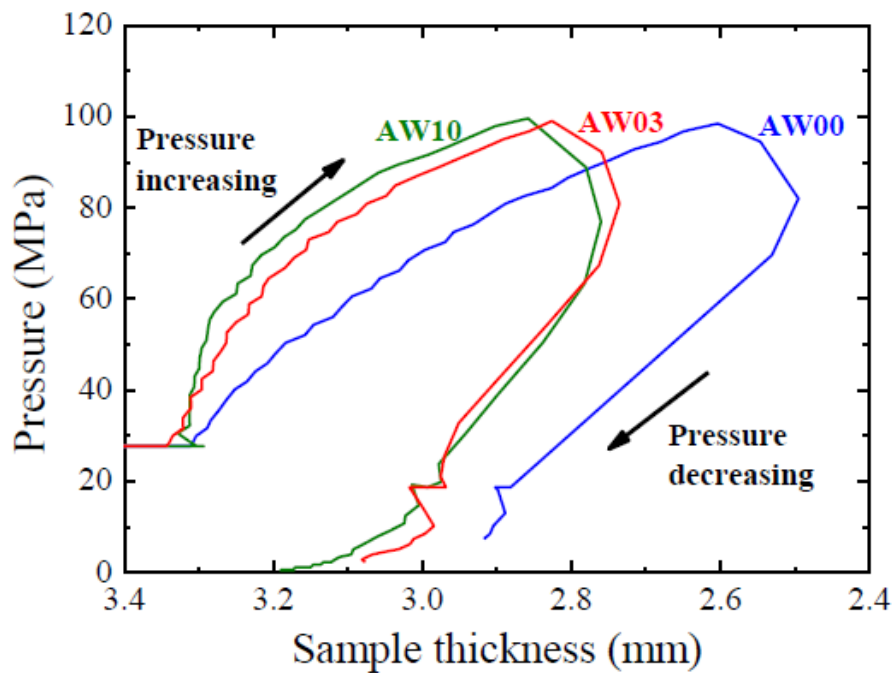
FIGURE 2.4

Fig.4: Compaction behavior of AW00, AW03 and AW10 powders at 1300 °C.

The sample thickness shown in Fig. 2.4 was calculated by sample thickness values measured during SPS minus the thermal expansion and elastic deformation data from blank test. As it is shown in Fig. 2.4, the final thickness of each sample is 2.99 mm for W00, 3.09 mm for W03, and 3.19 mm for W10. At the beginning, the sample thickness of W00, W03 and W10 were similar under a low pressure of 27MPa, the minimum contact pressure of SPS. The compaction during the pressure increment to 100MPa showed different behavior with the sequence of compaction AW00 > AW03 ≈ AW10 that certainly confirms that the addition of Al_2O_3 whisker hinders the densification of Al_2O_3 powder. The larger slope observed in W03 and W10 shrinkage plots up to 60 MPa indicates that the whiskers addition inhibits effectively the compaction of powders at low or moderate pressures. However, the slopes of W03 and W10 became similar to that of W00 above ⌣ 80 MPa, suggesting that whiskers do no longer influence sintering at larger pressures. During the unloading cycle and reduction from 100 to 80 MPa, compaction was still observed; while below 80 MPa no further compaction or densification was observed and displacement below 60 MPa correlates to the elastic response. It is important to point out that the compaction behavior and in consequence the densification response during SPS can be explained in terms of the larger diffusion distances in Al_2O_3 whisker-reinforced Al_2O_3 matrix ceramics rather than in pure ones.

Lower densification and grain growth suppression or reduction has been reported in CNT reinforced Al_2O_3 composites [14]. The origin of grain growth suppression relies on the fact that CNTs form two-dimensional mats on the Al_2O_3 grains and impede or partially block grain boundary diffusion [29]. However, in the case of

Al_2O_3 whiskers addition, a different phenomenon should take place, since Al_2O_3 whiskers are rigid, not flexible as CNTs, and cannot therefore form such unique mat-like structure. Since all interfaces in the composites are purely Al_2O_3-Al_2O_3 ones, the observed sintering behavior cannot be explained in terms of partial grain boundary diffusion suppression or blocking.

Differences in compaction behavior suggest that the particle rearrangement is affected by the whiskers addition, which is reasonable as the volume of Al_2O_3 whiskers is larger than that of the Al_2O_3 particles of the matrix. Furthermore, Al_2O_3 whiskers located around the Al_2O_3 matrix play a role as internal boundaries, which can reduce the internal stresses on the powder particles. Actually, densification of the powder matrix when surrounded by whiskers was inhibited and these zones remained porous after SPS as seen in Fig. 2(c) inset. As a result, grain growth was reduced by the internal stress decrease on the Al_2O_3 matrix. Because of this, relative density of AW10 remained below 97 % with a fine grained structure ($\leq 0.44 \mu m$) for all SPS conditions under a pressure of 75 MPa.

3.4. Mechanical properties

In order to eliminate the influence of porosity and grain size on hardness and fracture toughness, the three AW00, AW03 and AW10 ceramics with close relative density around ~97% and similar grain size of 0.35-0.44 µm were chosen to study the mechanical properties. The results of Vickers indentation tests are listed in Table 2.

Table 2.

Composition	Sintering temperature (°C)	Dwell time (min)	Hardness, H_v (GPa)	Standard deviation of H_v	Fracture toughness, K_{Ic} (MPa·m$^{1/2}$)	Standard deviation of K_{Ic}	Relative density (%)	Grain size, d (μm)
AW00	1200	3	26.7	1.6	4.25	0.22	97.9	0.35
AW03	1300	1	25.9	1.1	5.75	0.31	97.2	0.44
AW10	1400	3	23.4	1.4	4.72	0.28	96.9	0.44

Table 2. Room-temperature mechanical properties and microstructural features of selected AW00, AW03, and AW10 ceramics fabricated by SPS.

AW00 sintered at 1200 ºC for 3 min with relative density of 97.9% has the highest hardness (26.7 GPa). AW03 (SPSed at 1300 ºC for 1 min with relative density of 97.2%) has a similar hardness value (25.9 GPa) as AW00. The value of hardness reduces slightly by the addition of a higher content of whiskers for AW10 sintered at 1400 ºC for 3 min with relative density of 96.9% (23.4 GPa). On the other hand, the addition of 3 wt% of Al_2O_3 whiskers improves the toughness approximately ~30%, from 4.2 to 5.6 MPa $m^{1/2}$, while the addition of 10 wt% of Al_2O_3 whiskers shows a mild improvement to 4.7 MPa $m^{1/2}$ which is results of higher chance of whiskers accumulations (Fig. 3(b)) and less effective toughening mechanisms. Therefore, small loadings of Al_2O_3 whiskers (3 wt %) retain the hardness while improving the toughness by ~30%.

Enhanced fracture toughness K_{IC} of AW03 confirms the pieces of evidence of a well-dispersion and toughening mechanisms by whiskers, and in particular of crack bridging through whisker pullout observed in fracture surfaces (Fig. 3 (a)). Moreover, hardness and toughness of AW03 were larger than those of AW10. This suggests that the addition of whiskers in excess of 3wt% increases the number and extension of highly-concentrated whisker networks (Fig. 3(b)), increasing local porosity, which is unfavorable for mechanical properties.

To sum up, low content (~3 wt%) whiskers-reinforced alumina composites exhibit an optimal combination of high density and fine-grained microstructure and retain the high hardness of alumina with enhancement of toughness by ~30%. Mechanical properties of AW03 (H_v 25.9 GPa and K_{IC} 5.57 MPa $m^{1/2}$) were comparable or mostly higher than those of other alumina composites reported before, such as

67

TaC(20 vol%) – Al_2O_3 (H_v 17.4 GPa, K_{IC} 6.5 MPa m$^{1/2}$) [13], BN(20 vol%)– Al_2O_3 (H_v 26 GPa, K_{IC} 4.1 MPa m$^{1/2}$)[22], SiC particle(5 vol%) – Al_2O_3 (H_v 19 GPa, K_{IC} ⌣4 MPa m$^{1/2}$)[9], and SiC whiskers (20 vol%) – Al_2O_3 (H_v ⌣26 GPa, K_{IC} ⌣6 MPa m$^{1/2}$)[12]. However, Al_2O_3 whisker is the only secondary phase added to Al_2O_3 matrices that can prevent high temperature oxidation. Therefore, Al_2O_3 whiskers reinforcement of Al_2O_3 ceramics is a promising approach in order to get an Al_2O_3 "ceramic/composite" with improved mechanical properties under oxidizing atmospheres at high temperatures. However, future investigation is planned aimed at improving the dispersion of the Al_2O_3 whiskers throughout the Al_2O_3 matrix and removal of the residual porosity with the purpose of optimizing the high-temperature mechanical properties of an oxidation-resistant ceramic composite with real applications.

2.4. Conclusions: scientific achievements

This chapter is focused on Al_2O_3 whisker-reinforced alumina ceramics fabricated by SPS, especially to retain fine-grained microstructures and study the effect of whisker addition on the sintering behavior and room-temperature mechanical properties. It is found that sinterability of these alumina composites is retarded especially in higher whiskers content ones because whiskers hinder particle rearrangement and reduce internal stresses on the powder matrix. Nevertheless, fine-grained alumina ceramics could be obtained with relative density of 99% and grain size 0.45 μm for 3 wt % whiskers-added composites. For 10 wt % whiskers-added ones a relative density of ≥96% and grain size of 0.3- 0.44 μm are achieved by selecting proper SPS temperatures and dwell times (at 1300 ºC and 1400 ºC for 3 min, respectively).

Vickers hardness H_v of composite is comparable to that of pure alumina (26.7 GPa for monolithic alumina, 25.9 GPa for 3 wt% whisker addition, and 23.4 GPa for 10 wt%) whereas toughness K_{IC} increases (4.3 MPa m$^{1/2}$ for monolithic alumina, 5.57 MPa m$^{1/2}$ for 3 wt% whiskers-added ones, and 4.72 MPa m$^{1/2}$ for 10 wt%-added ones). Enhanced toughness is due to crack bridging induced by whiskers. To this purpose, a low amount of whiskers is found to be preferable to enhance mechanical properties.

References

[1] A. Okada, Automotive and industrial applications of structural ceramics in Japan, *J. Eur. Ceram. Soc.* 28 (2008)1097-1104.

[2] A. Krell, A new look at the influences of load, grain size, and grain boundaries on the room temperature hardness of ceramics, *Int. J Refract. Met. Hard Mater.* 16 (1998) 331-335.

[3] C. F. Gutierrez-Gonzalez, M. Suarez, S. Pozhidaev, S. Rivera, P. Peretyagin, W. Solis, L.A. Diaz, A. Fernandez, R. Torrecillas, Effect of TiC addition on the mechanical behavior of Al_2O_3-SiC whiskers composites obtained by SPS, *J. Eur. Ceram. Soc.* 36 (2016) 2149-2152.

[4] E. A. Olevsky, W. L. Bradbury, C. D. Haines, D. G. Martin, D. Kapoor, Fundamental Aspects of Spark Plasma Sintering: I. Experimental Analysis of Scalability, *J. Am. Ceram. Soc.* 95[8] (2012) 2406–2413.

[5] M. Demuyncka, J. P. Erauwa, O. Van der Biest, F. Delannay, F. Cambier, Densification of alumina by SPS and HP: A comparative study, *J. Eur. Ceram. Sci.* 32 (2012) 1957-1964.

[6] J. G. Santanach, A. Weibel, C. Estournès, Q. Yang, C. Laurent, A. Peigney, Spark plasma sintering of alumina: Study of parameters, formal sintering analysis and hypotheses on the mechanism(s) involved in densification and grain growth, *J. Eur. Ceram. Sci.* 59 (2011) 1400-1408.

[7] Y. Aman, V. Garnier, E. Djurado, Spark plasma sintering kinetics of pure α-alumina, *J. Am. Ceram. Sci.* 94 (2011) 2825-2833.

[8] K. T. Lee, S. I. Cha, K. T. Kim, K. H. Lee, S. H. Hong, Sintering behavior, microstructural evolution, and mechanical properties of ultra-fine grained alumina synthesized via in-situ spark plasma sintering, *Ceram. Int.* 42 (2016) 4290-4297.

[9] L. Gao, H. Z. Wang, J. S. Hong, H. Miyamoto, K. Miyamoto, Y. Nishikawa, S. D. D. L. Torreb, Mechanical properties and microstructure of nano-SiC-Al_2O_3 composites densified by spark plasma sintering, *J. Eur. Ceram. Soc.* 19 (1999) 609-613.

[10] Z. Y. Deng, J. L. Shi, Y. F. Zhang, D. Y. Jiang, J. K. Guo, Pinning effect of SiC particles on mechanical properties of Al_2O_3-SiC ceramic matrix composites, *J. Eur. Ceram. Soc.* 18 (1998) 501-508.

[11] S. S. Kumar, M. Devaiah, V.S. Bai, T. Rajasekharan, Mechanical properties of SiC_p/Al_2O_3 ceramic matrix composites prepared by directed oxidation of an aluminum alloy, *Ceram. Int.* 38 (2012) 1139-1147.

[12] G. D. Zhan, J. D. Kuntz, R. G. Duan, A. K. Mukherjee, Spark-Plasma Sintering of Silicon Carbide Whiskers (SiC_w) Reinforced Nanocrystalline Alumina, *J. Am. Ceram. Soc.* 87[12] (2004) 2297–300.

[13] G. Zhao, Ch. Huang, H. Liu, B. Zou, H. Zhu, J. Wang, Preparation of in-situ growth TaC whiskers toughening Al_2O_3ceramic matrix composite, *Int. J Refract. Met. Hard Mater.* 36 (2013) 122-125.

[14] F. Inam, H. Yan, T. Peijs, M. J. Reece, The sintering and grain growth behaviour of ceramic–carbon nanotube nanocomposites, *Comp. Sci. Tech.* 70 (2010) 947–952.

[15] N. Saheb, K. Mohammad, Microstructure and mechanical properties of spark plasma sintered Al2O3-SiC-CNTs hybrid nanocomposites, *Ceram. Int.* 42 (2016) 12330-12340.

[16] M. H. Bocanegra-Bernal, C. Dominguez-Rios, J. Echeberria, A. Reyes-Rojas, A. Garcia-Reyes, A. Aguilar-Elguezabal, Spark plasma sintering of multi-, single/double-

71

and single walled carbón nanotube-rainforced alumina composites: is it justifiable the effort to rainforce them?, *Ceram. Int.* 42 (2016) 2054-2062.

[17] E. Zapata-Solvas, D. Gómez-García, A. Domínguez-Rodríguez, Towards physical properties tailoring of carbon nanotubes-reinforced ceramic matrix composites, *J. Eur. Ceram. Soc.* 32 (2012) 3001-3012.

[18] J. Sun, L. Gao, W. Li, Colloidal processing of carbon nanotube/alumina composites, *Chem. Mater.* 14 (2002) 5169–72.

[19] K. Balani, T. Zhang, A. Karakoti, W. Z. Li, S. Seal, A. Agarwal, In situ carbon nanotube reinforcements in a plasma-sprayed aluminum oxide nanocomposite coating, *Acta. Mater.* 56 (2008) 571–579.

[20] S. W. Kim, W. S. Chung, K. S. Sohn, C. Y. Son, S. Lee, Improvement of flexure strength and fracture toughness in alumina matrix reinforced with carbon nanotube, *Mater. Sci. Eng. A.* 517 (2009) 293–299.

[21] K. Lee, C. B. Mo, S. B. Park, S. H. Hong, Mechanical and electrical properties of multi-walled CNT-alumina nanocomposites prepared by a sequential two step processing of ultrasonic spray pyrolysis and spark plasma sintering, *J. Am. Ceram. Soc.* 94 (2011) 3774–9.

[22] M. Hotta, T. Goto, Densification and microstructure of Al_2O_3–cBN composites prepared by spark plasma sintering, *J. Ceram. Soc. Jpn.* (2008) 116[6], 744-748.

[23] P. Klimczyk, M.E. Cura, A. M. Vlaicu, I. Mercioniu, P. Wyzga, L. Jaworska, S. –P. Hannula, Al_2O_3-cNB composites sintered by SPS and HPHT methods, *J. Eur. Ceram. Soc.* 36 (2016) 1783-1789.

[24] T. Isobe, D. Daimon, T. Sato, T. Matsubara, Y. Hikichi, T. Ota, Spark plasma sintering technique for reaction sintering of Al_2O_3/Ni nanocomposite and its mechanical properties, *Ceram. Int.* 34 (2008) 213–217.

[25] V. Valcárcel, A. Souto, F. Guitian, Development of Single-Crystal α-Al$_2$O$_3$ Fibers by Vapor-Liquid-Solid Deposition (VLS) from Aluminum and Powdered Silica, *Adv. Mater.* 10[2] (1998) 138-140.

[26] V. Valcárcel, A. Souto, F. Guitian, Method for Production of α-Alumina Whiskers via Vapor–Liquid–Solid Deposition, *J. Am. Ceram. Soc.* 86[10] (2003) 1683–90.

[27] G. B. Quinn, R. C. Bradt, On the Vickers indentation fracture toughness test, *J. Am. Ceram. Soc.* 90 (2007) 673–680.

[28] G. R. Anstis, P. Chantikul, B. R. Lawn, D. B. Marshall, A Critical Evaluation of Indentation Techniques for Measuring Fracture Toughness: I, Direct Crack Measurement, *J. Am. Ceram. Soc.* 64[9] (1981) 533-538.

[29] E. Zapata-Solvas, D. Gómez-García, A. Domínguez-Rodríguez, On the microstructure of single wall carbon nanotubes reinforced ceramic matrix composites, *J. Mater. Sci.* 45 (2010) 2258–2263.

Chapter 3

On the high-temperature plasticity of alumina-whisker-reinforced alumina

composites. Microstructural characterization. Modelling of the

deformation mechanisms.

Summary

The search of a competitive ceramic material for structural applications demands several requisites: a simple microstructure with easy reproducibility, good intrinsic mechanical properties and most of all, an optimal oxidation resistance. This later point is a challenging point for most ultrahigh refractory materials.

In this work an alumina (Al_2O_3) whisker-reinforced Al_2O_3 composite prepared by spark plasma sintering (SPS) is studied. It will be shown that, although the microstructure is quite similar to that of pure monolithic one, there is a notorious enhancement of the high-temperature deformation resistance, reaching up to one order of magnitude over the pure Al_2O_3 specimen. On the other hand, the activation energy of these composites increases notably. The results are explained in terms of an original model. A comparison with reported data shows that such composite is as efficient as a SiC-whisker-reinforced Al_2O_3 composite, with the advantage of its oxidation resistance and much less fabrication cost.

3.1. Introduction

Al_2O_3 ceramics are highly demanded as structural materials compared to other ceramic systems thanks to their excellent mechanical properties, such as a bending strength as high as 1300 MPa in three-point bending tests of nano-grained specimens [1], Vickers hardness of 25–30 GPa [2] and fracture toughness of 3-4 MPa m$^{1/2}$ in three point bending tests, depending on the microstructure [3]. Obviously, hardness, toughness and strength of Al_2O_3 could be improved via microstructural refinement [1-4]. Attempts to toughen Al_2O_3 by the addition of secondary phases in the form of particles or whiskers/fibers, such as SiC particles – Al_2O_3 [5-7], SiC whisker – Al_2O_3 [8], TaC whisker – Al_2O_3 [9], carbon nano tube (CNT) – Al_2O_3 [10], BN – Al_2O_3 [11], and metal – Al_2O_3 [12], have also been studied extensively.

Al_2O_3-based composites with high oxidation resistance have special interest for high-temperature structural applications. To this end, high-temperature mechanical behavior of Al_2O_3 composites have been also studied intensively [13], such as Al_2O_3-ZrO_2 [14-18], Al_2O_3-$Y_3Al_5O_{12}$ [19,20], Al_2O_3-SiC [21-24], and Al_2O_3- carbon nanotubes (CNT) [25,26]. Two different strategies have been adopted: one is focused on the fabrication of superplastic Al_2O_3composites with other oxides such as ZrO_2 [14-18] and the other option is the design of more creep resistant Al_2O_3 composites by addition of non-oxide secondary phases like SiC whiskers, carbon nanofibers or graphene oxide [25, 27]. The second strategy is more challenging because non-oxide phases usually have better creep resistance at high temperatures. Unfortunately, oxidation of these non-oxide secondary phases cannot be avoided. In fact, this is very clear in the case of SiC-whisker-reinforced composites: the creep strain rates when tested in air are higher than

those measured under reducing atmosphere [21, 22]. Therefore, oxidation of secondary phases can restrict the range of Al_2O_3 applications, which limits the validity of the alternative approach based upon improvement the mechanical performance of Al_2O_3 by addition of a non-oxidic second phase. In order to overcome this limitation, we have proposed that Al_2O_3 whisker-reinforced fine-grained Al_2O_3 ceramic composites can be a promising alternative material for technological applications. In fact, it already exhibits notorious room temperature mechanical properties [28]. Regarding their potential use at high temperatures, the advantage of Al_2O_3 whisker-reinforced Al_2O_3 ceramics is its intrinsic oxidation resistant character. However, there is no information on the creep resistant and degree of plasticity of these composites. This work pretends to cover this gap: the aim of this study is the analysis of the high-temperature deformation behavior of Al_2O_3-whisker reinforced Al_2O_3 ceramics, providing a comparison of the creep resistance between these whisker-reinforced Al_2O_3 ceramics and commonly-used SiC whisker-reinforced Al_2O_3 composites with well-known mechanical performance at high temperatures.

3.2. Experimental procedure

α-Al_2O_3 powder (Sumitomo Chemical Co., Ltd, Tokyo, Japan) of > 99.99 % purity, with particle size of $0.3 - 0.5$ μm and BET surface area of $5 - 10$ m^2/g. Al_2O_3 whiskers (Neoker, S. L., Milladoiro, Spain) of > 5 μm in length and aspect ratio 3:1 were used as raw materials. The physical features of alumina powders and the fabrication procedure of the whiskers are reported elsewhere [29]. Two Al_2O_3-Al_2O_3 whisker composites, one doped with 3 vol% whiskers and the other with 10 vol% were prepared and compared with pure Al_2O_3 ceramics. Hereafter, samples made of pure

Al$_2$O$_3$ powder are labelled as AW00, composites with 3 vol% whiskers and composites with 10 vol% whiskers as AW3 and AW10, respectively. In order to get a homogeneous mixture, they were subjected to ball-milling in a shaker mill with Si$_3$N$_4$ balls for 24 h in ethanol. The choice of these balls is based on the stability of them, i.e. they do not show any damage after milling. Later on, the resulting slurry was dried on a hot plate in air. Densification was carried out by means of a spark plasma sintering (SPS) furnace (Dr. Sinter SPS-515S, Fuji Electronic Industrial Co., Ltd., Kanagawa, Japan), using a graphite mold with inner diameter of 15 mm. Temperature of the graphite mold surface was monitored by an optical pyrometer and the SPS pulse sequence was set to 12:2. Optimal processing conditions, microstructural features and density of the samples measured by the Archimedes method in distilled water are listed in Table 1. Further details of the experimental procedure are described elsewhere [28].

Table 1

Composition	Optimal SPS conditions				Relative density (%)	Mean grain size (μm)
	Temperature (°C)	Time (min)	Heating rate (°C/min)	Pressure (MPa)		
AW00	1200	3	200	75	97.9	0.35
AW03	1250	3	200	100	96.3	0.41
AW10	1300	3	200	100	95.6	0.36

Table 1. Optimal fabrication parameters and microstructural features of the AW00, AW03 and AW10 ceramics prepared in this study. These conditions optimize the final density of the specimens. However, it is important to emphasize that any of the conditions is valid for the three sets of specimens.

78

Parallelepiped samples of about 4 mm × 2 mm × 2 mm were prepared for creep tests. Compressive creep tests were carried out at constant loads in-between 25-750 MPa in air at 1050 - 1350 °C while monitoring the instantaneous sample length *l* versus time *t*. Load jumps at fixed temperature enables to determine the stress exponent *n*, and temperature jumps at constant load permits to determine activation energy *Q*, assuming the phenomenological Harper-Dorn equation for high-temperature creep [30, 31].

$$\dot{\varepsilon} = A \frac{Gb}{kT} \left(\frac{\sigma}{G} \right)^{n} D_0 \exp\left(- Q\beta\right) \tag{1}$$

Where *n* and *Q* are the stress exponent and the activation energy respectively, D_0 is the pre-exponential factor of a diffusion coefficient, *G* is the shear modulus, σ and *T* are the applied stress and the temperature respectively, k is the Boltzmann's constant, b is a typical length of the microstructure (for instance, the Burgers vectors of dislocations in the material of the lattice parameter) and β=1/kT. Finally, *A* is a non-dimensional empirical constant which depends on the microstructure.

Sintered and deformed samples were polished by standard diamond polishing techniques with a surface finish of 1 μm. Polished samples were thermally treated at 1200 °C for one minute with heating rate of 20 °C/min and cooling rate 10 °C/min. Scanning electron microscope observation was carried out on polished-gold-coated sample by using a field-emission scanning electron microscopy (FE-SEM) (HITACHI S5200, Hitachi High-Technologies, Tokyo, Japan). The equivalent planar diameter *d* was measured from SEM photographs of random locations on the samples, counting more than 300 grains. Statistical analysis was made using Origin Pro 8 (Origin Lab, Northampton, USA). Transmission electron microscope (TEM) observation was carried

out on deformed specimens using TEM (PHILIPS CM-200, Philips, Eindhoven, Holland).

3.3. Results and discussion

High-temperature deformation of AW03 was observed in the temperature range of 1050 – 1250 ℃ under stresses in the range between 46 – 300 MPa. On the contrary AW10 did not show any plastic response below 1200 ℃: the specimen catastrophic failure occurred at 1200 ℃ at a stress level of 455 MPa. Creep deformation of AW10 was performed successfully in the temperature range of 1250 – 1350 ℃ under stresses of 45 – 165 MPa. Fig. 1 shows selected typical creep curves of load jump tests at 1250 ℃ for (a) AW03 and (b) AW10, and temperature jump tests for (c) AW03 under an initial stress of 300 MPa and (d) AW10 of 65 MPa, respectively.
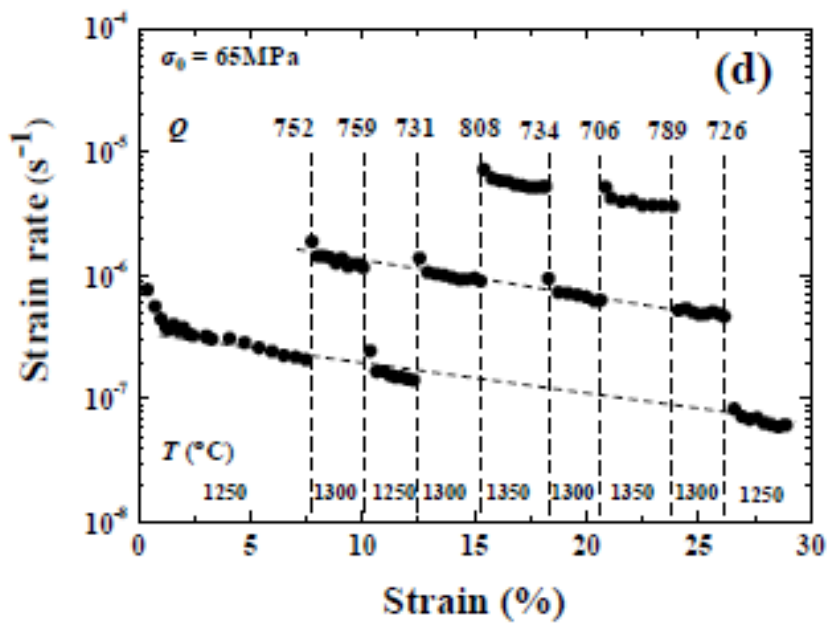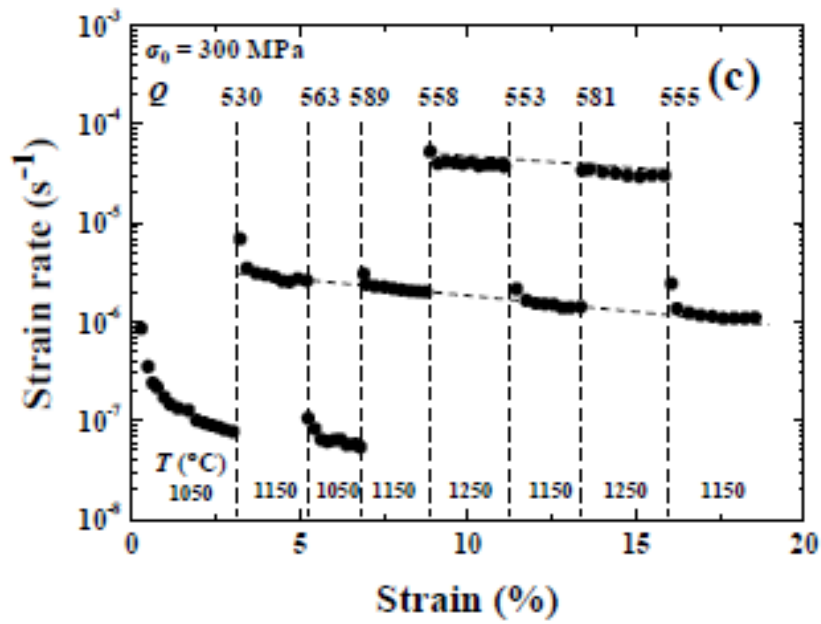
FIGURE 3.1
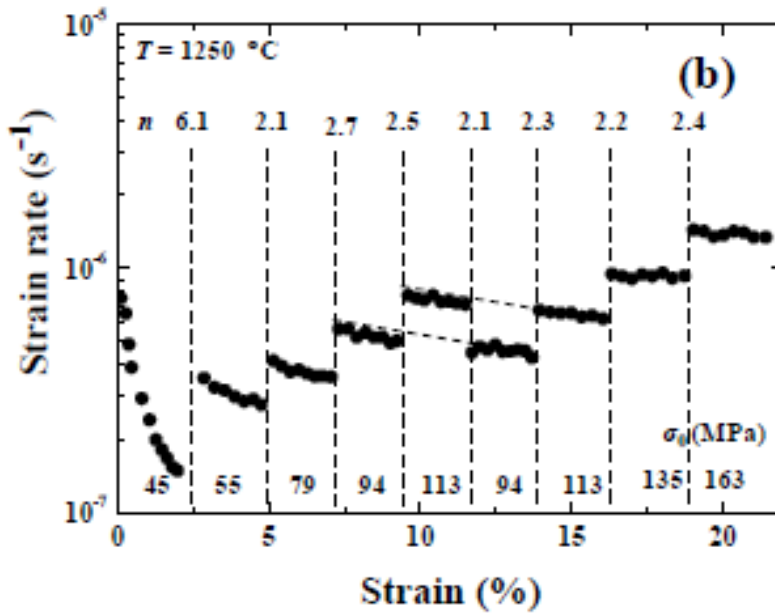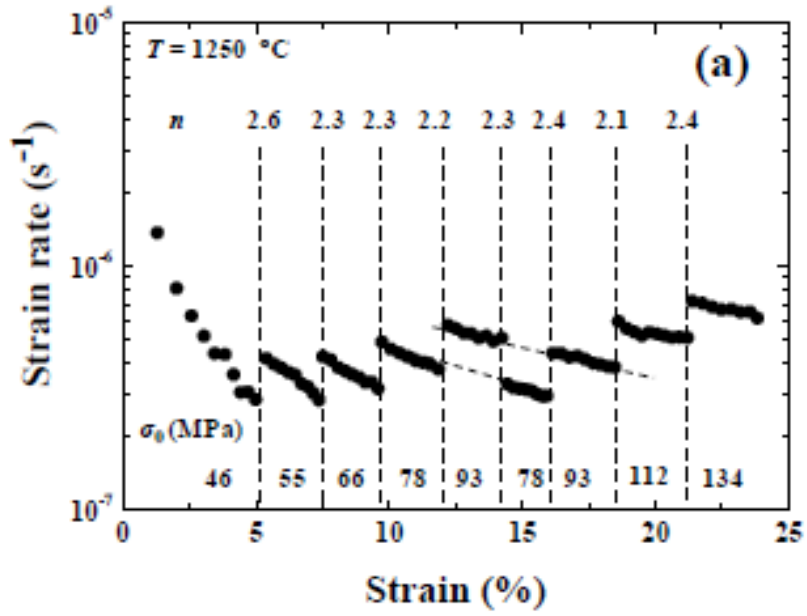
Fig. 3.1. Creep curves resulting from stress jump tests at 1250 °C for (a) AW03 and (b) AW10 and creep curves resulting from temperature jump tests at a fixed stress of 300 MPa for (c) W03 and 65 MPa for (d) W10.

Stress exponent *n* for each load jump and activation energy *Q* for each temperature jump calculated by equation 1 are reported in Fig. 1 (a, b) and (c, d), respectively. Similar deformation tests were carried out for pure Al_2O_3. They are not showed here because they are in full agreement with creep tests of fine-grained alumina made in a SPS device and quite recently reported in literature [32]. In all cases, the first stage shows only the specimen densification, especially for composites with the highest whisker content. Therefore, the value obtained from the first section is not reliable and they are not considered. The stress exponent values are systematically in the range of 2-2.7, while the activation energy exhibit different values: The higher the Al_2O_3 whisker content, the higher the value of *Q* (as an average, one can find Q_{AW00}=540±50 kJ/mol, Q_{AW03}=560±50 kJ/mol and Q_{AW10}=725±50 kJ/mol). The negative slope in all the segments is consistent with the sectional change of the specimen during constant load compression. A proof of this is the extrapolation of segments of stages at similar conditions but different ranges of strain, as displayed in Fig. 1. This is a mechanical proof of the fact that the microstructure does not evolve during deformation. The values of the activation energies and stress exponents in pure fine-grained alumina measured through creep tests have been reviewed in [32]. The stress exponents are in between 1.9-2.1, whereas the activation energies are in between 410-540 kJ/mol in compression. These values are consistent with those reported in our study.

Similar values of stress exponents and activation energies were reported previously for fine-grained pure Al_2O_3 reinforced with secondary phases and it was concluded that several deformation mechanisms can occur simultaneously or individually, such as diffusional creep, basal slip and/or accommodated or non-accommodated grain-boundary sliding [33-36]. It was shown that [33], although the stress exponent 2 was not affected by a second phase in Al_2O_3, the apparent activation energy of the creep was

83

found to increase from 520 kJ/mol for undoped Al_2O_3 till 760 kJ/mol for 1000 ppm zirconium-doped-Al_2O_3. Grain-boundary sliding accommodated by impurity-drag-controlled diffusion was suggested by these authors as a mechanism of deformation [33]. For SiC-whisker reinforced Al_2O_3 composites, values of n≥2 were currently found but with activation energies of ~700 kJ/mol, much higher than those measured in pure Al_2O_3 [34]. The authors [34] reported that the addition of non-deformable whiskers to the Al_2O_3 matrix inhibits the sliding of the grains below a certain threshold stress. For stresses over that value, sliding is possible, but as the transport of matter in the plastic Al_2O_3 is not fast enough to accommodate the microstructural constraints of the whisker network, damage can be subsequently formed. Formation of damage is more significant for larger volume fractions of whiskers [34]. The network of whiskers inhibits progressively the sliding of the grains. Plot of $\ln\dot{\varepsilon}$ vs $\ln\sigma$ of all experiments in the present study are reported in Fig. 3.2.
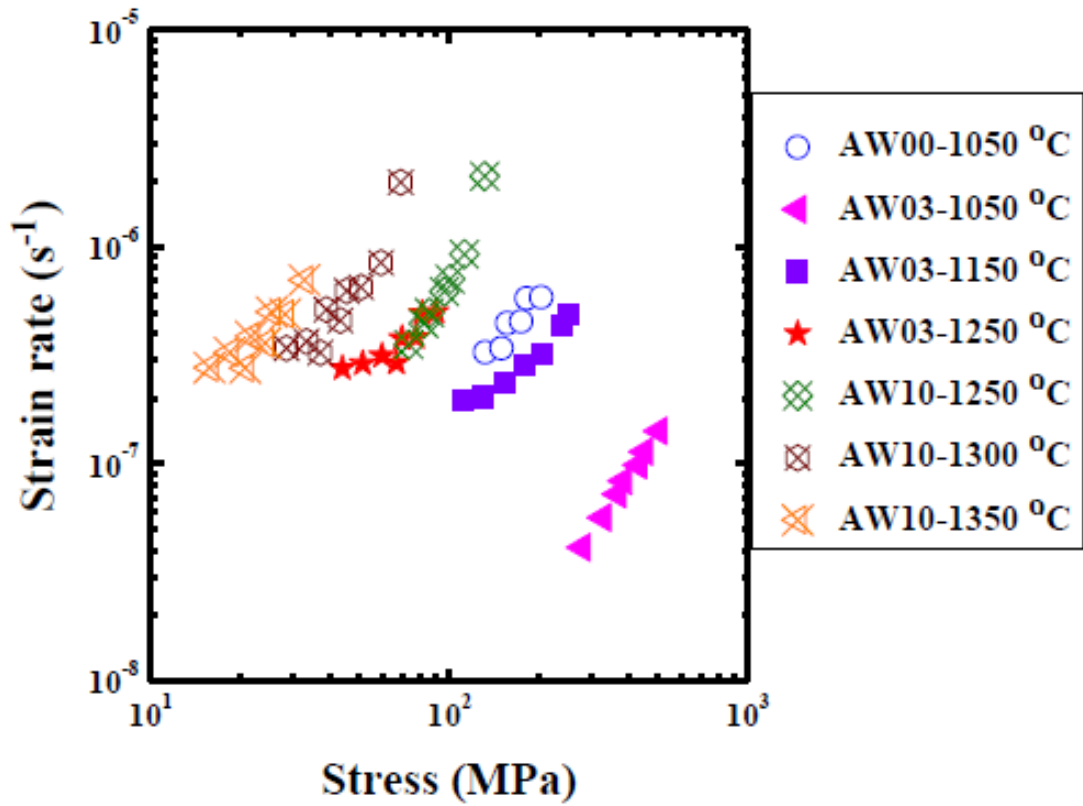
84

FIGURE 3.2

Fig. 3.2. Strain rate versus stress of all experiment sets.

As seen in Fig. 3.2, creep resistance of AW03 was enhanced in nearly one order of magnitude at 1050 ℃ compared to AW00, a change which is remarkable with merely the addition of 3 vol% Al_2O_3 whiskers. On the other hand, creep resistance of AW03 and AW10 were almost the same at 1250 ℃. In general terms, the increase in the Al_2O_3 whisker content restricts the grain sliding mobility. However, when the amount of whiskers is in excess of a certain whisker content amount, either cavitation and/or diffusional creep becomes favorable and the creep resistance decreases.

Grain sizes and grain shape factors of SPS-ed specimens and deformed ones were analyzed by SEM images and are reported in Table 2.

Table 2

Specimen condition		Grain size (µm)	Shape factor
AW00	SPS ed	0.35	0.80
	Deformed at 1050 °C	0.48	0.79
AW03	SPS ed	0.41	0.79
	Deformed at 1050 °C	0.45	0.77
	Deformed at 1150 °C	0.51	0.77
	Deformed at 1250 °C	0.60	0.77
AW10	SPS ed	0.36	0.78
	Deformed at 1250 °C	0.44	0.76
	Deformed at 1300 °C	0.49	0.77
	Deformed at 1350 °C	0.50	0.72

Table 2. Grain size and grain shape factor evolution of the AW00, AW03 and AW10 ceramics deformed at different temperatures.

Grain growth during creep test was moderate in AW03 and AW10, while the shape factor was almost similar after deformation indicating that grain boundary sliding is dominant. This is consistent with a nearly-invariant microstructure. TEM images of deformed specimens at 1250 ºC for AW03 and AW10 are shown in Figs. 3.3 (a) and (b), respectively.
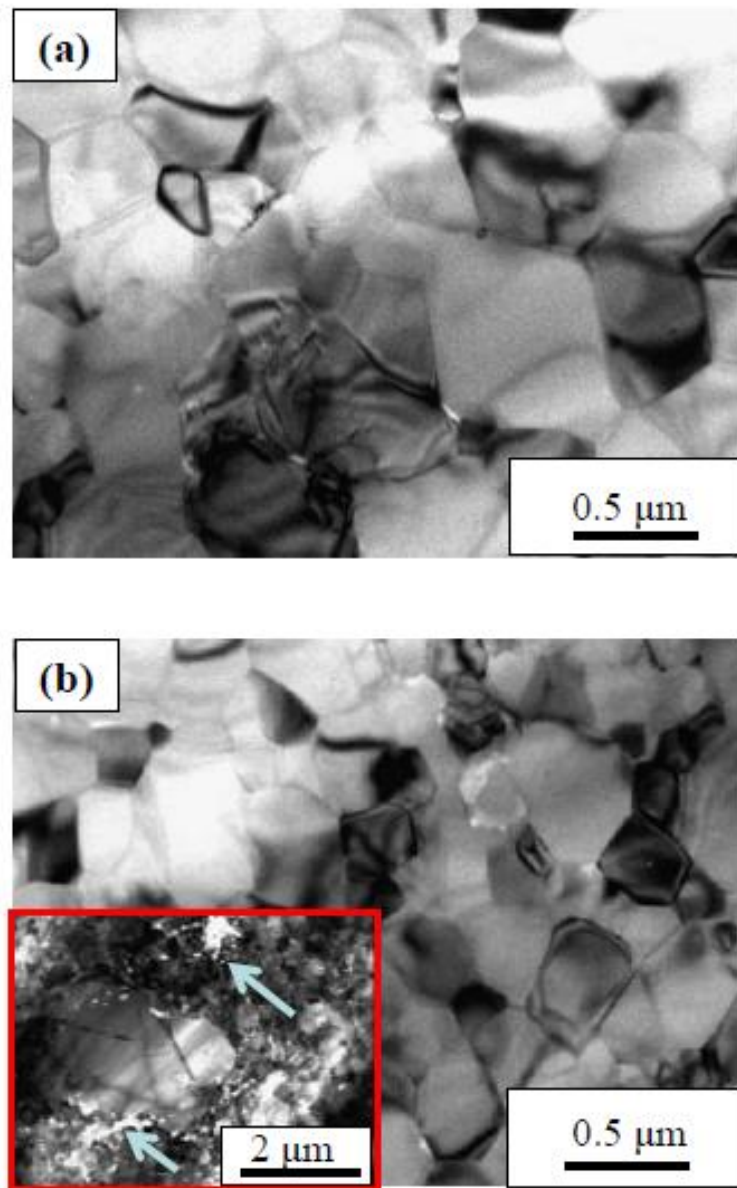
FIGURE 3.3

Fig. 3.3. Transmission electron micrographs of deformed specimens at 1250 ℃ for (a) AW03 and (b) AW10. The presence of cavities is indicated with arrows in inset of figure 3 (b).

Grain size of AW03 and AW10 in TEM images was consistent with the result of SEM observation. Cavitation opening is not remarkable for deformed AW03 specimen (Fig. 3(a)) while some cavitation along the grain boundaries can be observed in AW10 crept specimens (inset of Fig. 3 (b), meaning that for this composition the grain accommodation during deformation requires cavitation. The appearance of cavitation during creep deformation is a fact which was reported in literature [32, 37]. This is consistent with one microstructure in which alumina whiskers block grain motion remarkably, a fact which will be assessed theoretically later on. Finally there is no clear evidence of networks of dislocations in none of the deformed specimens.

The assessment of a homogeneous distribution of whiskers into the matrix cannot be validated by TEM or SEM and unfortunately it cannot be carried out by Raman spectroscopy due to the common crystallographic structure of whiskers and alumina grains. However, it is reasonable to think that the distribution is mostly homogenous because the specimens show a uniform plastic deformation.

A simple phenomenological model can be proposed to account for the two main experimental features: first, the creep resistance (defined as the ratio of strain rates measured in one tested composite and the strain rate in pure Al_2O_3 at the same temperature and stress conditions) increase; second, the remarkable activation energy increment with the whisker content.

Let us assume that deformation is mainly controlled by grain boundary sliding. Therefore, the strain rate must be proportional to the number of mobile grains in the specimen. We will make the hypothesis that whiskers are rigid structures with no mobility. We will assume also that compatibility between grains is maintained by diffusion accommodation. Obviously, the neighboring grains around one whisker have

88

a very limited mobility. We will introduce into the model one phenomenological length which we will call as the "correlation length" and it will be identified as λ. It is defined as the radius of the sphere centered in the whisker center of gravity in which all grains inside the sphere "feels" the influence of the whisker and their mobility is very restricted. Since the volume concentration of whisker is known, which can write as "c" from now on, the volume fraction of mobile grains f (proportional to the creep strain rate) can be calculated easily after a straightforward algebra:

$$f(\dot{\varepsilon}_{GBS}) = 1 - \frac{4}{3}\frac{\lambda^3(\dot{\varepsilon}_{GBS})}{r^2 L}c = 1 - \frac{4}{3}\left(\frac{\lambda}{L}\right)^3\left(\frac{L}{r}\right)^2 c \qquad (2)$$

Where r and L are the radius and the length of a whisker, assuming the geometry of a cylinder. It is very reasonable to conclude that the strain rate in a whisker-reinforced Al$_2$O$_3$ composite ($\dot{\varepsilon}_W$) should be proportional to f, i.e. $\dot{\varepsilon}_W = \frac{G_0}{G_c}f\dot{\varepsilon}_0 + \dot{\varepsilon}_D = \dot{\varepsilon}_{GBS} + \dot{\varepsilon}_D$, where $\dot{\varepsilon}_0$ is the strain rate measured in a pure Al$_2$O$_3$ specimen, G$_c$ is the shear modulus of the composite, G$_0$ is the shear modulus of pure alumina and $\dot{\varepsilon}_D$ is the contribution of diffusional creep which can be present when grain boundary sliding cannot be operative. In general terms, the correlation length must be a weakly-dependent quantity of the strain rate. If the strain rate interval of the creep tests is narrow and $\dot{\varepsilon}_w << 1$ (as happens in most cases) it is reasonable to assume a linear dependence such as $\lambda(\dot{\varepsilon}) = L - a\dot{\varepsilon}_{GBS}$ where "a" is a numerical constant (with $a\dot{\varepsilon}_{GBS} << 1$. Notice that the quantity "a" must be positive because the correlation length reduces when all grains gain a significant mobility, as happens when grain-boundary sliding increases. The analytical dependence proposed for $\lambda(\dot{\varepsilon}_{GBS})$ is the first term of the Taylor expansion of a possibly complex law which can be determined by finite element simulation methods

89

only. However, despite this crude simplification, the addition of higher-order terms does not change the conclusions of this model. On the contrary, it increases the mathematical treatment in an unnecessary way with no better accuracy. Therefore, they will be ignored. Taking into account these assumptions, a long but straightforward calculation allows obtaining the following expression for the activation energy:

$$Q \cong \frac{\alpha}{\alpha + f_0} Q_0 + \frac{1}{2} \frac{Q_0}{\alpha + f_0} \left(f_0 + \sqrt{f_0} \right) \tag{3}$$

Where $Q_0 = -\dfrac{\partial \ln \dot{\varepsilon}_D}{\partial \beta}$ is the activation energy measured in pure alumina specimens, $f_0 = f(0)$ and $\alpha = \dot{\varepsilon}_D \bigg/ \dfrac{G_0}{G_c} \dot{\varepsilon}_0$. The mathematical details are fully discussed in the appendix.
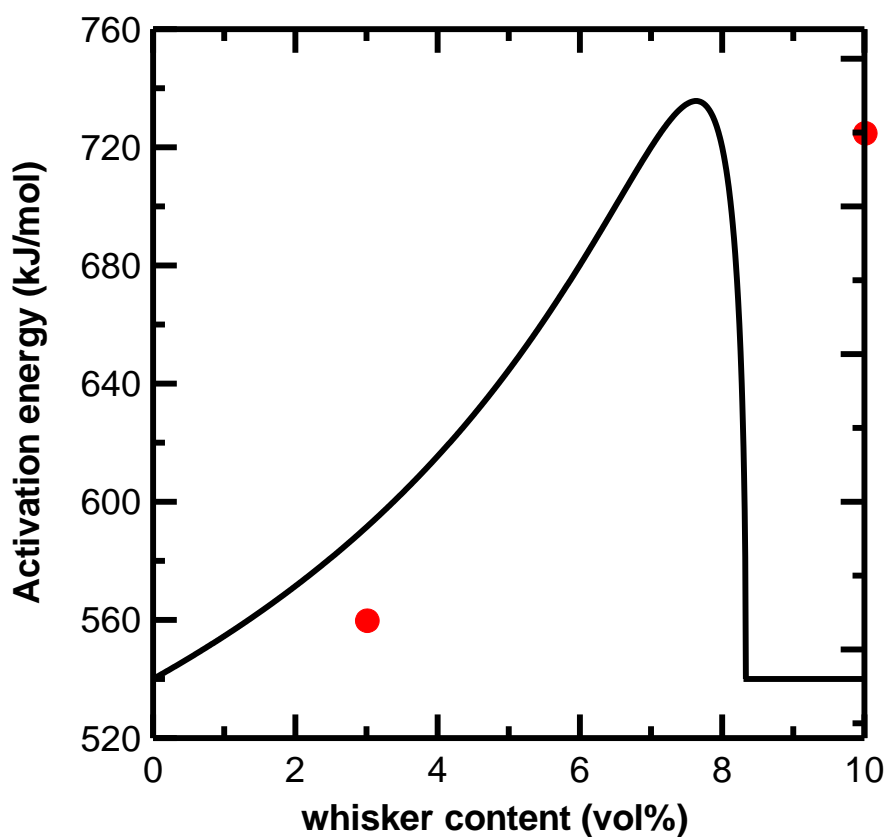
FIGURE 3.4

Fig. 3.4. Theoretical dependence of the activation energy versus the whisker content.

Experimental values (open circles) are superposed to the theoretical curve.

Figure 3.4 displays the theoretical value of Q versus the whisker content dependence. The experimental values (in red) obtained in this work are displayed for comparison.

Roughly, the tendency is correct. However, the predictions would be excellent if the real whisker amount were approximately 2 vol% less than the nominal value. One plausible explanation arises: whiskers may be partially agglomerated, a possibility which cannot be discarded, although it is not observed with the experimental techniques available for this study. In addition to that, the abrupt decrease of the activation energy values

towards Q_0 takes place at a whisker concentration approximately equal to 8%. This value is the concentration at which all alumina grains "feel" the blocking effect of whiskers. When it happens, deformation can be fulfilled through non-accommodated or partially-accommodated diffusional creep. An obvious consequence of this is the nucleation of cavities at the boundaries. Moreover, the creep resistance decreases, in good agreement with the experimental tendency.

Future studies with more sets of composites with different whisker concentrations would permit to assess the validity of this statement and evaluate the theoretical model proposed here.

However, although the model is rather crude, it can explain the origin of the activation energy increase in whisker-reinforced composites. To our knowledge, there is no alternative explanation in literature, except speculative statements invoking grain boundary diffusion and/or cavitation.

With respect to the increase of creep resistance, the model predicts that it depends mostly on the increase of the shear modulus. This statement seems reasonable if we pay attention to the mixture law and the remarkable value of the shear modulus in alumina whiskers [40].

The creep resistance comparison between Al_2O_3 reinforced by Al_2O_3 whiskers and SiC-whisker-reinforced Al_2O_3 is displayed in Fig. 5 (AW03 versus 30 vol% SiC whisker reinforced Al_2O_3 taken from the literature [21, 24]). These data were collected under similar conditions as this study: 1250°C; uniaxial compression; stress range 25–200 MPa while deformation was under Ar atmosphere and whiskers with similar shape ratio.
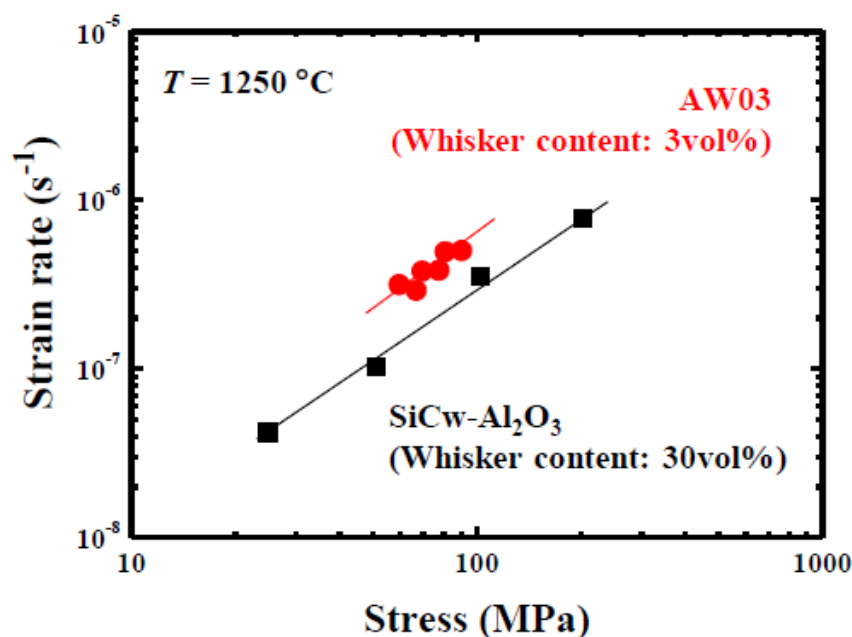
92

FIGURE 3.5

Fig.3.5. Strain rate versus stress of alumina whisker-reinforced alumina ceramics
(AW03) and SiC whisker-reinforced alumina [24].

According to these data, the incorporation of SiC whiskers in Al_2O_3 gives rise to an enhancement of creep resistance which is almost comparable to that obtained with the addition of Al_2O_3 whiskers. This is even more remarkable if attention is paid to the fact that the grain size in SiC-whisker-reinforced composites is 1.5 µm, much higher than the values considered in this work. In both Al_2O_3-SiC and Al_2O_3- Al_2O_3 whiskers composites, a partial blocking of grain-boundary sliding by either SiC [24] or Al_2O_3 whiskers, respectively, seems to occur. Therefore, it seems that the creep resistance of whisker-reinforced composites mainly depends on the amount and shape factor of whiskers, the chemical nature of them being not so essential (provided glassy phases are not formed). This is valid as long as whiskers are sufficiently rigid, exhibit no plasticity and the deformation mechanism of the composite is grain boundary sliding.

From a practical point of view, a remarkable advantage of the composite considered in this work is the fact that Al_2O_3 whiskers can improve the creep resistance impressively without high temperature oxidation and degradation and it is the easiest and cheapest option to this purpose. In fact, the costs of fabrication are reduced significantly if Al_2O_3 whiskers are chosen instead of SiC or other non-oxide phases. In addition to that, no glassy phases are formed at the boundaries, a point which is rather important when searching for a good creep performance at high temperatures. Therefore, Al_2O_3-whisker-reinforcement of Al_2O_3 ceramics is a promising approach in order to get an Al_2O_3 ceramic composite with improved mechanical properties under oxidizing atmospheres at high temperatures with competitive perspectives in technological applications.

3.4. Conclusions and scientific achievements

An Al_2O_3 composite composed of Al_2O_3 whiskers have been fabricated by spark plasma sintering. The microstructure is a homogeneous distribution of equiaxial grains in which whiskers are embedded into them. High-temperature tests show that the creep resistance improves up to one order of magnitude compared to the pure Al_2O_3 specimen when the whisker content is merely around 3 vol%. Under this circumstance, this composite is as efficient as others reported in literature in which a second phase of SiC is elected. Considering the strong oxidation resistance of Al_2O_3, the composite described in this paper is proposed as an alternative cheap option for high-temperature structural applications under an oxidizing atmosphere conditions. From a basic point of view, one simple model has been proposed to explain the significant increase of the activation energy during creep. The model explains in a partially quantitative way the

94

experimental results, but more studies are required to validate for a wide range of composites with different whisker concentrations.

References

[1] J. Koike, S. Tashima, S. Wakiya, K. Maruyama, H. Oikawa, Mechanical properties and microstructure of centrifugally compacted Al_2O_3 and hot-isostatically-pressed Al_2O_3, Mat. Sci. Eng. A 220 (1996) 26-34.

[2] A. Krell, Fracture Origin and Strength in Advanced Pressureless-Sintered Al_2O_3, J. Am. Ceram. Soc. 81 (1998) 1900-1906.

[3] A. Krell, S. Schadlich, Nanoindentation hardness of submicrometer Al_2O_3 ceramics, Mat. Sci. Eng. A 307 (2001) 172–181.

[4] A. Krell, A new look at the influences of load, grain size, and grain boundaries on the room temperature hardness of ceramics, Int. J. Refract. Metal. Hard Mater. 16 (1998) 331-335.

[5] L. Gao, H. Z. Wang, J. S. Hong, H. Miyamoto, K. Miyamoto, Y. Nishikawa, S. D. D. L. Torre, Mechanical Properties and Microstructure of Nano-SiC-Al_2O_3 Composites by Spark Plasma Sintering, J. Eur. Ceram. Soc. 19 (1999) 609-613.

[6] Z. Y. Deng, J. L. Shi, Y. F. Zhang, D. Y. Jiang, J. K. Guo, Pinning Efect of SiC Particles on Mechanical Properties of Al_2O_3-SiC Ceramic Matrix Composites, J. Eur. Ceram. Soc. 18 (1998) 501-508.

[7] S. Santhosh Kumar, M. Devaiah, V. Seshu Bai, T. Rajasekharan, Mechanical properties of SiCp/Al_2O_3 ceramic matrix composites prepared by directed oxidation of an aluminum alloy, Ceram. Int. 38 (2012) 1139-1147.

[8] G. D. Zhan, J. D. Kuntz, R. G. Duan, A. K. Mukherjee, Spark-Plasma Sintering of Silicon Carbide Whiskers (SiC_w) Reinforced Nano crystalline Al2O3, J. Am. Ceram. Soc. 87 (2004) 2297-2300.

[9] G. Zhao, C. Huang, H. Liu, B. Zou, H. Zhu, J. Wang, Preparation of in-situ growth TaC whiskers toughening Al_2O_3 ceramic matrix composite, Int. J. Refract. Metal. Hard Mater. 36 (2013)122–125.

[10] F. Inam F, H. Yan; T. Peijs; M. J. Reece, The sintering and grain growth behaviour of ceramic–carbon nanotube nanocomposites, Comp. Sci. Tech. 70 (2010) 947–952.

[11] M. Hotta, T. Goto, Densification and microstructure of Al_2O_3–cBN composites prepared by spark plasma sintering, J. Jpn. Ceram. Soc. 116 (2008) 744-748.

[12] T. Isobe, K. Daimon, T. Sato, T. Matsubara, T. Hikichi, T. Ota, Spark plasma sintering technique for reaction sintering of Al_2O_3/Ni nanocomposite and its mechanical properties, Ceram. Int. 34 (2008) 213-217.

[13] Q. Tai, A. Mocellin, Review: High temperature deformation of Al_2O_3-based ceramic particle or whisker composites, Ceram. Int. 25 (1999) 395-408.

[14] F. Wakai; H. Kato, S. Sagaguchi, N. Murayama, Compressive deformation of Y_2O_3-stabilized ZrO_2/Al_2O_3 composite, J. Jpn. Ceram. Soc. 94 (1986) 1017-1020.

[15] B. J. Kellett, F. F. Lange, Hot forging characteristics of fine-grained ZrO_2 and Al_2O_3/ZrO_2 ceramics, J. Am. Ceram. Soc. 69 (1986) C172-C173.

[16] J. Wang, R. Raj, Interface effects in superplastic deformation of Al_2O_3 containing zirconia, titania or hafnia as a second phase, Acta. Metal. Mater. 39 (1991) 2909-2919.

[17] J. M. Calderon-Moreno, Influence of ZTA content on the compressive deformation in the Al_2O_3-ZrO_2 (12 mol% CeO_2) system, Key. Eng. Mater. 132-136 (1997) 2088-2091.

[18] L. Clarisse, R. Baddi, J. Bataille, A. Crampon, R. Duclos, J. Vicens, Superplastic deformation mechanisms during creep of Al2O3-zirconia composites, Acta. Mater. 45 (1997) 3843-3853.

[19] J. D. French, J. Zhao, M. P. Harmer, H. M. Chan, G. A. Miller, Creep of duplex microstructures, J. Am. Ceram. Soc. 77 (1994) 2857-2865.

[20] H. Duong, J. Wolfenstine, Creep behaviour of fine-grained two-phase Al_2O_3-$Y_3Al_5O_{12}$ materials, Mater. Sci. Eng. A. 172 (1993) 173-179.

[21] A. D. De Arellano-Lopez, F. L. Cumbrera, A. Dominguez-Rodriguez, K. C. Goretta, J. L. Routbort, Compressive creep of SiC-whisker-reinforced Al_2O_3, J. Am. Ceram. Soc. 73 (1990) 1297-1300.

[22] P. Lipetzky, S. R. Nutt, D. A. Koester, R. F. Davis, Atmosphere effects on compressive creep of SiC-whisker-reinforced Al_2O_3, J. Am. Ceram. Soc. 74 (1991) 1240-1247.

[23] A. H. Swan, M. V. Swain, G. L. Dunlop, Compressive creep of SiC whisker-reinforced Al_2O_3, J. Eur. Ceram. Soc. 10 (1992) 317-326.

[24] A. R. De Arellano-Lopez, A. Dominguez-Rodriguez, K. C. Goretta, J. L. Routbort, Plastic deformation mechanisms in SiC-whisker-reinforced Al_2O_3, J. Am. Ceram. Soc. 76 (1993) 1425-1432.

[25] E. Zapata-Solvas, R. Poyato, D. Gómez-García, A. Domínguez-Rodríguez, V. Radmilovic, N. P. Padture, Creep-resistant composites of Al_2O_3 and single-wall carbon nanotubes, Appl. Phys. Lett. 92 (2008) 111912.

[26] E. Zapata-Solvas, D. Gómez-García, R. Poyato, Z. Lee, M. Castillo-Rodríguez, A. Domínguez-Rodríguez, V. Radmilovic, N. P. Padture, Microstructural Effects on the Creep Deformation of Al_2O_3/Single-Wall Carbon Nanotubes Composites, J.Am.Ceram.Soc. 93 (2010) 2042-2048.

[27] R. Cano-Crespo, B. M. Moshtaghioun, D. Gómez-García, A. Domínguez-Rodríguez, R. Moreno, High-temperature creep of carbon nanofiber-reinforced and

graphene oxide-reinforced Al_2O_3 composites sintered by spark plasma sintering, Ceram. Int. 43, 15 (2017) 7136–7141.

[28] Y. Tamura, B. M. Moshtaghioun, D. Gomez-Garcia, A. Dominguez-Rodriguez, Spark plasma sintering of fine-grained Al_2O_3 ceramics reinforced with Al_2O_3 whiskers, Ceram. Int. 43 (2017) 658-663.

[29] V. Valcárcel, C. Cerecedo, F. Guitián, Method for production of α-alumina whiskers via vapour-liquid-solid deposition, J. Am. Ceram. Soc. 86 (2003) 1683-90.

[30] J. Poirier, Creep in Crystals, Cambridge University Press, Cambridge, United Kingdom, 1985.

[31] G. S. Corman, High-Temperature Creep of Some Single Crystal Oxides, Ceram. Eng. Sci. Proc. 12 (1991) 1745-1766.

[32] B. Ratzker, M. Sokol, S. Kalabukhov, N. Frage, Using a spark plasma sintering apparatus as a tool in a compressive creep study of fine-grained alumina, Ceram. Int.43 (2017) 9369-76.

[33] F. Wakai, T. Nagano, T. Iga, Hardening in creep of Al_2O_3 by zirconium segregation at the grain boundary, J.Am.Ceram.Soc. 80 (1997) 2361-6.

[34] A. R. de Arellano, A. Domínguez-Rodríguez, J. L. Routbort, Microstructural constraints for creep in siC-whisker-reinforced Al_2O_3, Acta. Mater. 46 (1998) 6361-6373.

[35] R. M. Cannon, W. H. Rhodes, and A. H. Heuer, Plastic Deformation of Fine-Grained alumina (Al_2O_3): I, Interface-Controlled Diffusional Creep, J.Am. Ceram. Soc. 63 (1980) 46–53.

[36] A. H. Heuer, N. J. Tighe, and R. M. Cannon, Plastic Deformation of Fine-Grained alumina (Al_2O_3): II, Basal Slip and non-accommodated Grain Boundary Sliding, J. Am. Ceram. Soc. 63 (1980) 53–58.

[37] J. Chevalier, C. Olagnon, G. Fantozzi & H. Gros, Creep Behaviour of Alumina, Zirconia and

Zirconia-Toughened Alumina, J. Eur. Ceram. Soc. 17 (1997) 859-64

[38] M. F. Ashby, R. A. Verrall, Diffusion-accommodated flow and superplasticity, Acta metal. 21 (1973) 149-163.

[39] A. H. Chokshi, An evaluation of the grain-boundary sliding contribution to creep deformation in polycrystalline alumina, J. mater. Sci. 25 (1990) 3221-28.

[40] J. Cook, Mechanical testing of whiskers, Composites, (1970), 176-180.

Appendix

Mathematical demonstration of equation (3) displayed in the main text.

The strain rate of the composite can be written as:

$$\dot{\varepsilon}_w = \dot{\varepsilon}_{GBS} + \dot{\varepsilon}_D = \frac{G_0}{G_c} f\dot{\varepsilon}_0 + \dot{\varepsilon}_D \tag{A.1}$$

The physical meaning of this equation is the following one: $\dot{\varepsilon}_D$ is the diffusional creep contribution to the full deformation, which is present whether the grain is blocked or not. This quantity does not depend on the shear modulus of the composite. On the other hand, the grain-boundary sliding contribution to the full strain rate is represented by $\dot{\varepsilon}_{GBS}$. This quantity depends on the nature of the material (i.e. the mobility of alumina grains), it must be proportional to the ratio of free grains in the bulk and it is inversely proportional to the shear modulus. The term $\dot{\varepsilon}_0$ is the strain rate of a pure alumina polycrystal. The term f f is the ratio of non-blocked grains and $\frac{G_0}{G_c}$ is the correction of shear moduli; i.e. G_0 is the shear modulus of pure alumina whereas G_c is the shear modulus of the composite. This correction is important for the grain-boundary sliding mechanism because the strain rate is inversely proportional to this quantity. On the contrary, it is not important for diffusional creep, because no grain slide operates in this case.

By application of the conventional definition of the activation energy, one can write:

101

$$Q = -\frac{\partial \ln \dot{\varepsilon}_w}{\partial \beta} = -\frac{\dot{\varepsilon}_{GBS}}{\dot{\varepsilon}_w}\frac{\partial \ln \dot{\varepsilon}_{GBS}}{\partial \beta} - \frac{\dot{\varepsilon}_D}{\dot{\varepsilon}_w}\frac{\partial \ln \dot{\varepsilon}_D}{\partial \beta} = -\frac{\dot{\varepsilon}_{GBS}}{\dot{\varepsilon}_w}\frac{\partial \ln \dot{\varepsilon}_{GBS}}{\partial \beta} + Q_0\frac{\dot{\varepsilon}_D}{\dot{\varepsilon}_w}$$

(A.2)

This expression can be developed if we take into account that $\dot{\varepsilon}_{GBS} = \dfrac{G_0}{G_c}f\dot{\varepsilon}_0$. Indeed,

the grain-boundary sliding contribution can be expressed as:

$$\frac{\partial \ln \dot{\varepsilon}_{GBS}}{\partial \beta} = \frac{\partial \ln \dot{\varepsilon}_0}{\partial \beta} + \frac{\partial \ln f}{\partial \beta} = -Q_0 + 3\frac{f-1}{f}\frac{\partial \ln \lambda}{\partial \ln \dot{\varepsilon}_{GBS}}\frac{\partial \ln \dot{\varepsilon}_{GBS}}{\partial \beta}$$

(A.3)

Finally, if we remember that $\lambda = L - a\dot{\varepsilon}_{GBS}$ a closed expression for $\dfrac{\partial \ln \dot{\varepsilon}_{GBS}}{\partial \beta}$ can be

proposed. Firstly:

$$\frac{\partial \ln \lambda}{\partial \ln \dot{\varepsilon}_{GBS}} = \frac{\dot{\varepsilon}_{GBS}}{\lambda}\frac{\partial \lambda}{\partial \dot{\varepsilon}_{GBS}} = \frac{\lambda - \lambda_0}{\lambda}$$

(A.4)

Where $\lambda_0 = \lambda(0)$

Therefore:

$$\frac{\partial \ln \dot{\varepsilon}_{GBS}}{\partial \beta} = -\frac{Q_0}{1 + 3\dfrac{1-f}{f}\left[1 - \left(\dfrac{1-f_0}{1-f}\right)^{1/3}\right]} \cong -\frac{Q_0}{1 - \dfrac{1-f}{1-f_0}\dfrac{f-f_0}{f}}$$

(A.5)

In this last equation (A.5), the Taylor expansion of the denominator has been applied,

because $\dfrac{f-f_0}{f_0} << 1$. This is a consequence of the weak dependence of $\lambda(\dot{\varepsilon}_{GBS})$.

Finally, substituting (A.5) into (A.3), a final expression of Q can be obtained:

$$Q = Q_0 \frac{\dot{\varepsilon}_{GBS}}{\dot{\varepsilon}_w} \frac{1}{1 - \dfrac{1-f}{1-f_0} \dfrac{f-f_0}{f}} + Q_0 \frac{\dot{\varepsilon}_D}{\dot{\varepsilon}_w} = Q_0 \frac{\alpha}{f+\alpha} + Q_0 \frac{f}{f+\alpha} \frac{1}{1 - \dfrac{1-f}{1-f_0} \dfrac{f-f_0}{f}} =$$

$$= Q_0 \frac{\alpha}{f+\alpha} + Q_0 \frac{f}{f+\alpha} F(f, f_0)$$

(A.6)

$$\text{With } \alpha = \frac{\dot{\varepsilon}_D}{\dfrac{G_0}{G_c} \dot{\varepsilon}_0} \text{ and } F(f, f_0) = \frac{1}{1 - \dfrac{1-f}{1-f_0} \dfrac{f-f_0}{f}}$$

(A.7)

According to the analysis of equation (A.1), α is the ratio of the diffusional creep contribution compared to the grain-boundary sliding contribution of the composite. The value of this parameter is not essential in our model. In fact, it has been introduced just to remove the mathematical artifact which appears when $f_0 = 0$: if diffusional creep is ignored and grain boundary sliding is inhibited, the model would not predict plasticity at all and Q→∞. Obviously such divergency never occurs in real materials, because at least either diffusional creep or cavitation takes place. The model does not depend essentially on the values of α provided that α<1. Such quantity has been theoretically [38] and experimentally evaluated in literature [39]. In the first case, α~0.1-0.2. In the case of experimental data, they were measured in four-point bending tests at 1400ºC and α=0.4±0.1. We adopted a value of

α=0.25.

According to this analysis, the activation energy depends on both the whisker content and the grain-boundary strain rate, the second dependence being much weaker. In order to describe the whisker content dependence, we are going to average the strain-rate dependence as follows:

First, it is easy to check that $0 \le F(f, f_0) \le 1$ and $\left(\dfrac{\partial F}{\partial f} \right)_{f = \sqrt{f_0}} = 0$. It means that there

exists a maximum or minimum for $f = \sqrt{f_0}$. In fact, in this case it is a global maximum

for $f \in [0,1]$. This global maximum can be calculated by direct substitution of f by

$\sqrt{f_0}$ in A.7. The result is $F(\sqrt{f_0}, f_0) = \dfrac{1 + \sqrt{f_0}}{2\sqrt{f_0}}$ Therefore $F(f, f_0) \le \dfrac{1 + \sqrt{f_0}}{2\sqrt{f_0}}$.

Secondly, if this relationship is taken, it is possible to replace $F(f, f_0)$ by $F(\sqrt{f_0}, f_0)$

and an upper-bound value for the activation energy Q can be written as:

$$Q \cong Q_0 \frac{\alpha}{f_0 + \alpha} + Q_0 \frac{f_0}{f_0 + \alpha} \left(\frac{1 + \sqrt{f_0}}{2\sqrt{f_0}} \right) = Q_0 \frac{\alpha}{f_0 + \alpha} + \frac{1}{2} Q_0 \frac{1}{f_0 + \alpha} \left(f_0 + \sqrt{f_0} \right) \qquad \text{(A.8)}$$

Conclusions and prospective in this research line

This dissertation book reports the fabrication of alumina-fiber-reinforced alumina ceramics by means of spark plasma sintering (SPS). Prior to sintering, the optimized conditions for SPS sintering of both monolithic and composites have been identified. The hypothesis in mind for fabrication of these ceramics is the potential enhancement of mechanical properties of the composites with regard to those of monolithic species. The mechanical testing and microestructural characterization of samples prior to and post-mortem reveals two main facts: first, the Vickers hardness is essentially unaltered when compared with alumina specimens with the same average grain size. However, the fracture toughness is significantly improved due to the crack-bridging effects of the alumina fibers in the composites. Second, regarding the high-temperature plasticity, the physical mechanism is grain-boundary sliding, a fact which is also a common feature in monolithic specimens. However, the creep resistance is remarkable improved, being comparable to that provided by a high amount of SiC fibers in alumina matrix.

The main conclusion which can be learned from this research work is twofold: from a practical point of view, the use of alumna-fiber alumina composites can be economically attractive because handling of alumina powders and fibers of the same chemical nature is by far easier than mixing two phases of different ceramics. The reader can bear in mind all the drawbacks derived from the presence of grain boundaries acting as a border of two different materials. Not to say if the second phase is susceptible of oxidation at high temperatures. In this sense, the composites studied here are more competitive than other presumably more exciting ones, such as nanotube or graphene-based ones.

From a basic point of view a key question arises: which are the ingredients required for the improvements of the mechanical performance of a composite? At first

sight, this thesis suggests that only three: the elastic constants of the fiber and the matrix, the morphology of the fibers and the spatial arrangements of these fibers inside the matrix. The chemical nature of the fibers does not seem to be so critical. But now there is a challenging task to be elucidated: determining the morphology of the fibers and the distribution in the matrix for optimization of the mechanical properties. Going further into this problem demands a huge effort on modeling of the stress fields inside the composites and experimental assessment. For this research plan, alumina-alumina ceramics can be a model system for evaluation of analythical or numerical models.

In this context, other researchers have just made sounded contributions. For instance, Prof. Uematsu and co-workers, from Nagaoka University [1], have fabricated a grain-oriented alumina ceramics by means of colloidal processing under high magnetic fields. The resulting material has excellent optical and mechanical properties. Such strategy can be useful for fiber orientation in our composites for the search of better mechanical performant ceramics and a reply on the role of the fiber arrangement when embedded into the matrix.

In addition to this, another strategy to pursue in this research field is the fabrication of similar systems with fibers of the same chemical nature as the matrix. At this regard, SiC-fiber-reinforced SiC ceramics have been partially explored only [2].

REFERENCES

[1]-Antoine Pringuet , Takuma Takahashi, Shoko Baba, Yuta Kamo, Zenji Kato, Keizo Uematsu, Satoshi Tanaka, Fabrication of Transparent Grain-Oriented Polycrystalline Alumina by Colloidal Processing, J. Am. Ceram. Soc. 99 (10) 3217-19, October 2016.

[2]-S.Zhua, M.Mizuno, Y.Kagawa, Y.Mutoha, Monotonic tension, fatigue and creep behavior of SiC-fiber-reinforced SiC-matrix composites: a review, Composites Sci. and Tech. 59 (6), 833-51, May 1999.

PUBLICATIONS IN JCR JOURNALS BASED UPON THIS DISSERTATION

1-Yoshihiro Tamura, Bibi Malmal Moshtaghioun, Diego Gomez-Garcia, Arturo Domínguez Rodríguez, Spark plasma sintering of fine-grained alumina ceramics reinforced with alumina whiskers, Ceramics International, Volume 43, Issue 1, Part A, January 2017, Pages 658-663.

2-Yoshihiro Tamura, Bibi Malmal Moshtaghioun, Eugenio Zapata-Solvas, Diego Gomez-Garcia, Arturo Domínguez-Rodríguez, Carmen Cerecedo-Fernández, Víctor Valcárcel-Juárez,

Is an alumina-whisker-reinforced alumina composite the most efficient choice for an oxidation-resistant high-temperature ceramic? Journal of the European Ceramic Society, Volume 38, Issue 4, April 2018, Pages 1812-1818.

3-Yoshihiro Tamura, Eugenio Zapata-Solvas, Bibi Malmal Moshtaghioun, Diego Gómez-García, Arturo Domínguez-Rodríguez, Grain-boundary diffusion coefficient in α-Al2O3 from spark plasma sintering tests: Evidence of collective motion of charge disconnections, Ceramics International, in press, corrected proof, available online from 9 July 2018. (https://doi.org/10.1016/j.ceramint.2018.07.073).